Performance Modeling of the Baffled Tube Ram Accelerator

Cullen Yancey

A thesis
submitted in partial fulfillment of the
requirements for the degree of

Master of Science in Aeronautics and Astronautics

University of Washington

2022

Reading Committee:

Carl Knowlen, Chair

Dana Dabiri

Program Authorized to Offer Degree:
Aeronautics and Astronautics

University of Washington

Abstract

Performance Modeling of the Baffled Tube Ram Accelerator

Cullen Yancey

Chair of the Supervisory Committee:
Chair Carl Knowlen

The baffled tube ram accelerator is a hypervelocity mass driver theoretically capable of accelerating axisymmetric projectiles up to 3 km/s. Researchers at the UW have investigated the baffled tube ram accelerator since 2015 achieving projectile velocities over 1.4 km/s. The device is based on the smooth bore ram accelerator developed at the UW in the 1980s and consists of washer-like inserts normal to the flow that are used to prevent unstart and enable the use of axisymmetric projectiles and more energetic propellants. With baffled tubes, the ram accelerator is theoretically capable of achieving 2-3 times more thrust than the smooth bore ram accelerator. Theoretical performance models including three drag models with combustion effectiveness were developed and compared with experiment. The results show that only 35-65% of the theoretical thrust is observed in baffled tube ram accelerator experiments, although thrust is still improved over the smooth bore ram accelerator. Performance losses may be attributed to momentum lost to baffle drag, which hinders performance in most experiments, but may provide a boost to performance at low Mach numbers.

TABLE OF CONTENTS

LIST OF FIGURES

LIST OF TABLES

GLOSSARY

Variable List

A: Area, m^2

V: Volume, m^3

L: Length, m

d: diameter, m

β: Effective area ratio

F: Thrust, N

D: Drag, N

I: Non-dimensional thrust

M: Mach number

a: Local sound speed, m/s

u: Velocity, m/s, km/s

p: Pressure, bar

ρ: Density kg/m^3

R: Mixture gas constant, $\frac{J}{kgK}$

T: Temperature, K

γ: Specific heat ratio

c_P: Specific heat at constant pressure, $\frac{kJ}{kgK}$

h: specific enthalpy, $\frac{kJ}{kg}$

Δh_f°: Enthalpy of formation, $\frac{kJ}{kg}$

Δq: Heat release, $\frac{J}{kg}$

Q: Non-dimensional heat release

c_D: Coefficient of drag

Ψ: Control volume length fraction

$\dot{m}$: Mass flow rate, kg/s

$\dot{Q}$: Rate of heat release, kg/s

η_c: Combustion efficiency

ϕ: Equivalence ratio

Subscripts and Superscripts

1: Entrance plane

2: Exit plane

a: Annulus

b: Tube bore

c: Chamber

eff: Effective

SBRA: Smooth Bore Ram Accelerator

BTRA: Baffled Tube Ram Accelerator

CJ: Chapman-Jouguet

max: Maximum

Imax: Peak non-dimensional thrust

ACKNOWLEDGMENTS

First, a huge thank you to Dr. Carl Knowlen for the opportunity to join the Ram Accelerator Lab and for the endless knowledge you've imparted on me over the past year. For most students, it's not every day you get to work with a living, breathing ram accelerator encyclopedia, but that was my life. I admire your dedication to this project and I'm incredibly grateful for the guidance you've given me on my journey.

A special thanks to Dr. Dana Dabiri for serving on my thesis committee and providing intriguing insights from the perspective of someone who's not constantly enveloped by ram.

To my fellow grad students, John, Brian, Desiree, and Jason, it's been a privilege to work with you. I've learned so much from each of you and I can't wait to welcome you all to the ram alumni crew soon! To all of the undergrads, you make the ram world go round. One day we'll have Dirty Jobs shoot an episode on cleaning the catcher tube and you'll get all the glory.

To Addison, a thank you doesn't even begin to repay the immeasurable support you've given me over the last year and a half. I'm extremely grateful to have had you by my side and I will happily share all the praise with you. To my parents, siblings, and the rest of my family and friends, I hope you take so much pride in this work. I'm only able to accomplish what I have because of your support over the past 25 years.

Finally, thank you to HyperSciences Inc. for their support of the UW Ram Accelerator lab and to the US Air Force for providing me the with an incredible opportunity to return to school.

DEDICATION

to my siblings Nolan, Madalyn, and Braden ...

Chapter 1
INTRODUCTION

The ram accelerator is a hypervelocity launch concept with the capability to accelerate projectiles to orbital velocities. Researchers at the University of Washington (UW) developed the technology in the mid-1980s and have successfully achieved muzzle velocities > 2.6 km/s.[1] Ram accelerator operation differs from gun operation in that the energy release process, and therefore the region of highest pressure, travels with the projectile. Through staging and scaling, the ram accelerator has the potential to accelerate projectiles greater than 1000 kg to velocities greater than 6 km/s.[2, 3] Staging enables control of the energy density of the propellant, the acceleration profile of the projectile, and the sound speed of the mixture.[4] Scalability has been proven with successful operation of projectiles ranging from $0.1 - 4.3$ kg in tube bores ranging from 12.7-mm to 120-mm in diameter.[5, 6] The UW ram accelerator facility will be discussed in Chapter 3.

1.1 Thermally Choked Ram Accelerator

Ram accelerators generate thrust via a propulsive cycle similar to that of a conventional airbreathing ramjet engine.[7] With a conventional ramjet engine, shown in Fig. 1.1, supersonic air is compressed and decelerated to subsonic velocity through series of shock waves beginning at the engine inlet. Then, fuel is injected for combustion in the subsonic region before the flow is accelerated out a nozzle to generate thrust.

In the thermally choked ram accelerator (TCRA), shown in Fig. 1.2, a subcaliber projectile resembling a ramjet centerbody is fired down a stationary tube that acts

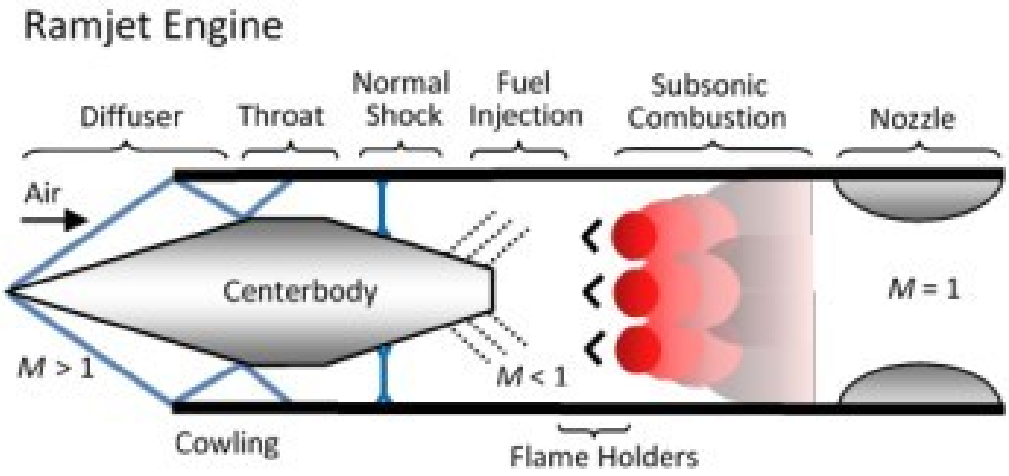

Figure 1.1: A conventional ramjet engine's propulsive cycle.

like a ramjet engine cowling. Ram accelerator operation necessitates having supersonic flow at the point of largest projectile cross-sectional area, or maximum area constriction. The projectile travels through pre-mixed fuel and oxidizer such that no propellant is carried on board the projectile. Subsonic combustion occurs at the base of the projectile, which acts as a flameholder, resulting in thrust.

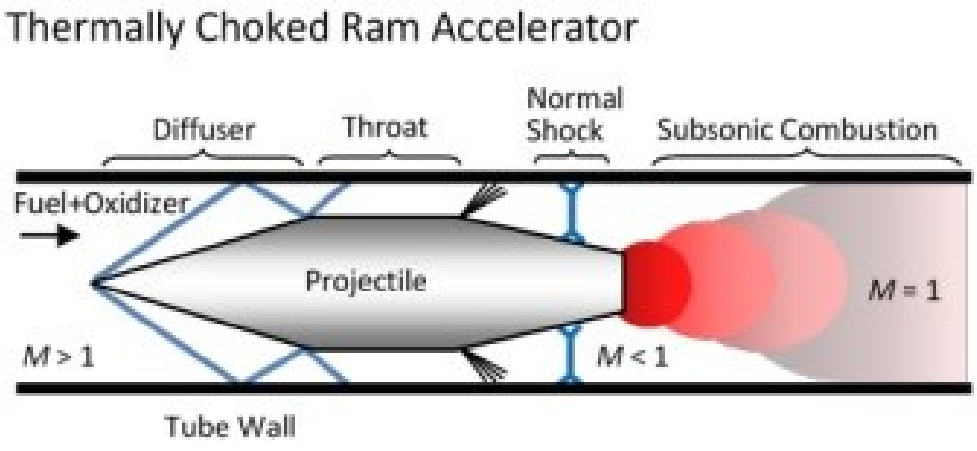

Figure 1.2: The thermally choked ram accelerator propulsive cycle.

1.2 Baffled Tube Ram Accelerator

In 2005, a new concept called the baffled tube ram accelerator (BTRA) was conceived to alleviate some of the obstacles encountered during the first two decades of experiments.[8] The BTRA has been studied extensively at UW since 2015 and has the theoretical capability to accelerate axisymmetric projectiles to muzzle velocities of 3 km/s. Figure 1.3 shows a section view of a baffled tube containing washer-like inserts that serve to keep combustion waves from overtaking the projectile and causing a total loss of thrust. The BTRA enables the use of axisymmetric projectiles and expansion of the ram accelerator's operational envelope by utilizing more energetic propellants. More energy dense propellants serve to improve thrust performance at a given fill pressure and reduces minimum starting velocity.[9]

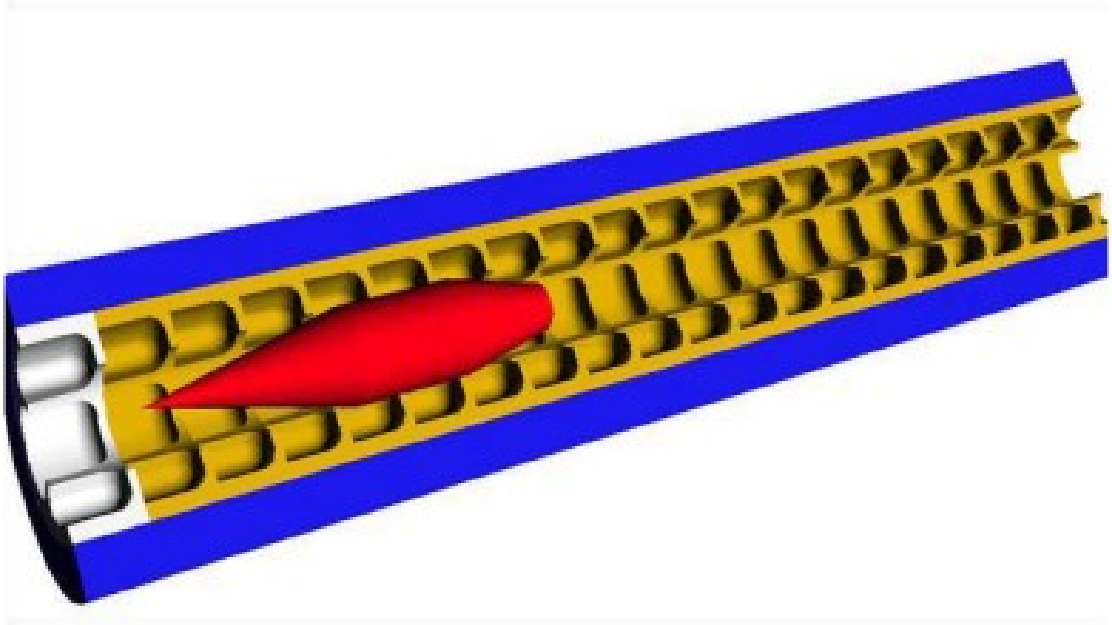

Figure 1.3: Section view of a projectile traveling through a baffled tube.

Ram accelerators can operate via thermal choking or mechanical choking as a

conventional ramjet engine does. Operation can occur in three velocity regimes: sub-detonative, trans-detonative, and super-detonative referring to the projectile velocity relative to the Chapman-Jouguet (CJ) detonation velocity.[10] The focus of this paper is on the TCRA, which necessarily operates in the sub-detonative velocity regime. TCRA operation in both smooth bore and baffled tube will be explained further in Chapter 2.

Modeling of the BTRA has proven challenging from a computational fluids standpoint and the one-dimensional model has been known to be lacking. The intent of this thesis is to examine options for incorporating baffle drag and addressing heat release issues related to performance and other factors into BTRA models. This is done with the hope of creating a model that, ultimately, will better represent experiment and enable rapid parameterization for BTRA designs to be used for a number of applications including direct space launch, drilling, and more. In this thesis, theoretical performance models will be described including three drag models and a model for combustion effectiveness for BTRA operation. Finally, these performance models will be adjusted to fit experimental data from recent 8-m BTRA experiments for comparison of the theoretical models with experimental results in Chapter 4.

Chapter 2
THEORETICAL MODELS

This chapter discusses the propulsive modes that define ram accelerator operation in the sub-detonative velocity regime along with three drag models and a combustion effectiveness adjustment that modify ram accelerator theoretical performance. The thermodynamics involved in the thermally choked propulsive mode will be applied to both smooth bore ram accelerator and baffled tube ram accelerator.

2.1 Thermally Choked Ram Accelerator

The thermally choked ram accelerator (TCRA) was the only propulsive mode investigated during the ram accelerator experiments analyzed in this thesis. When modeling the TCRA propulsive mode in the projectile frame of reference, propellants are ingested at the inlet of the TCRA control volume and are then compressed through a series of shocks along the projectile. Heat (energy) is added to the constant area tube via combustion near the base of the projectile causing an increase in pressure and the velocity of the combusted propellants to increase toward the local speed of sound at the exit plane of the control volume; i.e., $u_2 \rightarrow a_2$ such that $M_2 = 1$ with respect to the projectile.

The control volume used in this one-dimensional, quasi-steady analysis is bounded by Stations 1 and 2, the tube wall, and the projectile as shown in Fig. 2.1.

The exit of the control volume is marked by the thermally choked plane. For a given mass flux, entropy is a maximum at thermal choking. Furthermore, when chemical equilibrium of the combustion products is reached, entropy is also at a maximum. Thus, the thermally choked reactive flow is at an entropy maximum.[11]

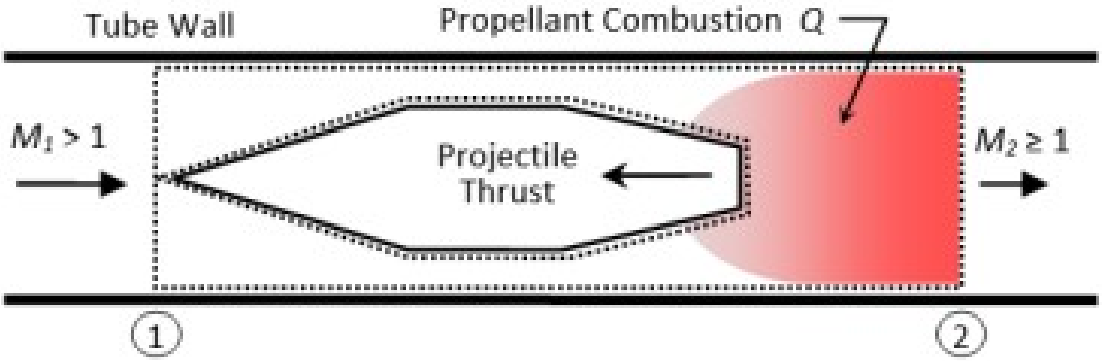

Figure 2.1: The TCRA Control Volume.

Therefore, the control volume in Fig. 2.1 encapsulates the entire thrust generation process and no details of the flow field within the control volume are necessary to determine thrust on the projectile.[12]

2.1.1 Smooth Bore Ram Accelerator

In a smooth bore ram accelerator (SBRA), a sub-caliber projectile is accelerated within a smooth tube. The entrance plane ① and the exit plane ② in Fig. 2.1 provide the only conditions necessary to analyze TCRA performance because the entrance and exit conditions represent the entropy minimum and maximum within the control volume.[12] Drag can be neglected in SBRA theory because of negligible friction on the tube walls, but will play a significant role later for the baffled tube ram accelerator.[13]. Non-dimensional thrust for the SBRA is derived as follows, beginning with the conservation of momentum applied to the control volume in Fig. 2.1, where F is projectile thrust.

$$F = \left(p_2 A_2 + \rho_2 u_2^2 A_2\right) - \left(p_1 A_1 + \rho_1 u_1^2 A_1\right) \tag{2.1}$$

Since area is constant at the entrance and exit planes of the control volume, thrust can be normalized by the fill pressure, p_1 and bore area, A_b.

$$\frac{F}{p_1 A_b} = \left(\frac{p_2}{p_1} + \frac{\rho_2}{p_1} M_2^2 a_2^2\right) - \left(1 + \frac{\rho_1}{p_1} M_1^2 a_1^2\right) \tag{2.2}$$

Assuming the propellants act as ideal gases, such that $p = \rho RT$, enables the substitution $\gamma = a^2 \frac{\rho}{p}$ where the speed of sound is defined as $a = \sqrt{\gamma RT}$.

$$\frac{F}{p_1 A_b} = \frac{p_2}{p_1}\left(1 + \gamma_2 M_2^2\right) - \left(1 + \gamma_1 M_1^2\right) \tag{2.3}$$

The pressure ratio, p_2/p_1, can be expressed using a combination of the ideal gas law, the equation for speed of sound, and the conservation of mass.

$$\frac{p_2}{p_1} = \frac{M_1}{M_2}\frac{\sqrt{\gamma_1 R_2 T_2}}{\sqrt{\gamma_2 R_1 T_1}} \tag{2.4}$$

Next, the conservation of energy applied to the TCRA control volume results in:

$$\rho_1 u_1 A_b \left(h_1 + \frac{u_1^2}{2} + \Delta q\right) = \rho_2 u_2 A_b \left(h_2 + \frac{u_2^2}{2}\right) \tag{2.5}$$

where $\Delta q = \Delta H_f^0$, the change in enthalpy of formation between the reactants and the products at $T_{ref} = 0$ K. By normalizing to the inlet conditions and using the ideal gas law, the following equation is obtained.

$$\frac{h_1}{c_{p1} T_1} + M_1^2 \frac{\gamma_1 - 1}{2} + Q = \frac{h_2}{c_{p1} T_1} + M_2^2 \frac{\gamma_2 - 1}{2}\frac{c_{p2} T_2}{c_{p1} T_1} \tag{2.6}$$

where Q is a non-dimensional heat release parameter that is useful for predicting performance of both the SBRA and BTRA and defined below.

$$Q = \frac{\Delta q}{c_{p1} T_1} = \frac{\Delta h_f^\circ}{c_{p1} T_1} \tag{2.7}$$

Solving Eq. 2.6 for the temperature ratio at the inlet and exit leads to:

$$\frac{T_2}{T_1} = \frac{c_{p1}}{c_{p2}}\left(\frac{\frac{h_1}{c_{p1} T_1} + M_1^2 \frac{\gamma_1 - 1}{2} + Q}{\frac{h_2}{c_{p2} T_2} + M_2^2 \frac{\gamma_2 - 1}{2}}\right) \tag{2.8}$$

Combining Eq. 2.8 with Eq. 2.4 and that result with Eq. 2.3 leads to:

$$\frac{F}{p_1 A_b} = \frac{M_1}{M_2}(1+\gamma_2 M_2^2)\frac{\gamma_1}{\gamma_2}\sqrt{\left(\frac{\gamma_2-1}{\gamma_1-1}\right)\left(\frac{\frac{h_1}{c_{p1}T_1}+\frac{\gamma_1-1}{2}M_1^2+Q}{\frac{h_2}{c_{p2}T_2}+\frac{\gamma_2-1}{2}M_2^2}\right)} - \left(1+\gamma_1 M_1^2\right) \quad (2.9)$$

Finally, the TCRA operating mode inherently means that the exit Mach condition, M_2, is unity resulting in:

$$I_{SBRA} = \frac{F}{p_1 A_b} = M_1(1+\gamma_2)\frac{\gamma_1}{\gamma_2}\sqrt{\left(\frac{\gamma_2-1}{\gamma_1-1}\right)\left(\frac{\frac{h_1}{c_{p1}T_1}+\frac{\gamma_1-1}{2}M_1^2+Q}{\frac{h_2}{c_{p2}T_2}+\frac{\gamma_2-1}{2}}\right)} - \left(1+\gamma_1 M_1^2\right) \quad (2.10)$$

Equation 2.10 describes the non-dimensional thrust produced in a SBRA via the thermally choked propulsive mode. Thus, non-dimensional thrust is a function of the thermodynamic parameters, γ and $\frac{h}{c_P T}$, and two independent parameters: projectile Mach number and non-dimensional heat release of the propellant. The thermodynamic parameters vary weakly with Mach number according to the chemical equilibrium code; their significance will be discussed later. Figure 2.2 shows three theoretical non-dimensional thrust curves for $1\,CH_4 + 2\,O_2 + 3\,N_2$, $1\,CH_4 + 2\,O_2 + 4.67\,N_2$, and $1\,CH_4 + 2\,O_2 + 7.52\,N_2$ using the thermodynamic parameters at the CJ Mach number.

The non-dimensional thrust-Mach profiles show that peak thrust, peak thrust Mach number, M_{CJ}, and therefore zero thrust Mach number all increase as a mixture becomes more energetic. Nearly all of the experiments reported here 30% oxygen-enriched air ($1\,CH_4 + 2\,O_2 + 4.67\,N_2$), which predicts $I_{max} = 8.3$ near $M_1 \approx 2.8$ and predicts zero thrust at $M_{CJ} = 5.65$. Ram accelerator operation at speeds greater than M_{CJ} requires transitioning to the super-detonative propulsive mode [2, 7], which does not adhere to TCRA theory and is not covered in this thesis.

The non-dimensional heat release in Eq. 2.7 is determined using the enthalpy of formation of the products minus the reactants at a reference temperature. The

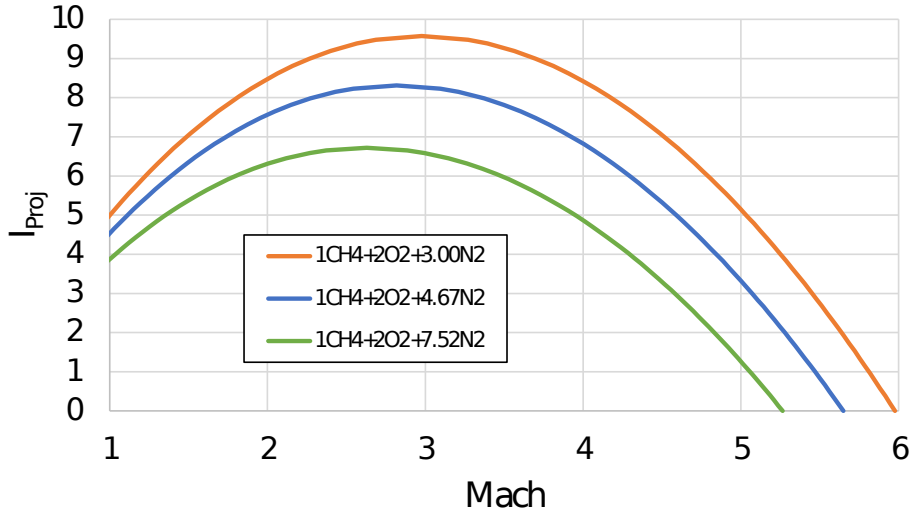

Figure 2.2: Theoretical ram accelerator performance for methane-air propellant at various N_2 dilution levels. The mixture becomes hotter with less N_2, increasing heat release and non-dimensional thrust.

chemical equilibrium code uses a reference temperature of 298 K, but a more accurate Q would be determined with reference to 0 K because specific enthalpy is referenced such that $h = 0$ J/kg when $T = 0$ K. Later Q will be determined as a function of M, I, γ, and $\frac{h}{c_P T}$. This Q will be based on the enthalpy of formation at 0 K and will be the Q used to calculate the drag and combustion effectiveness models.

2.1.2 Baffled Tube Ram Accelerator

The baffled tube ram accelerator (BTRA) is assumed to also operate with a thermally choked propulsive cycle and can theoretically accelerate projectiles up to 3 km/s.[9] The BTRA contains baffle inserts, which form a series of chambers separated by annular rings with rails connecting them for structural support and to help guide axisymmetric projectiles. Baffles are spaced such that a projectile blocks at least one baffle at all times as it travels through the test section. Essentially, the baffles act

as a one-way valve that allows propellant to be ingested into the control volume, but prevents the combustion wave from overtaking the projectile and causing an unstart. An unstart refers to the case when a ram projectile disgorges its normal shock wave ahead of itself. The shock wave is pushed forward by the projectile or a combustion wave, subjecting the projectile to subsonic flow, and therefore, ceasing ram operation.

Figure 2.3 gives insight into the flow field around the projectile as it travels through the BTRA test section. Upon entering a baffle chamber, the projectile ingests the premixed propellant and compresses it until the projectile shoulder eventually reaches the baffle, blocking it off. Each time the projectile passes through one of the annular rings, it unstarts, generating a normal shock ahead of its shoulder. If the projectile overtakes the normal shock before it reaches the next baffle chamber, the ram process is restarted. Successful operation throughout the test section means that this unstart-restart process occurs repeatedly.[14]

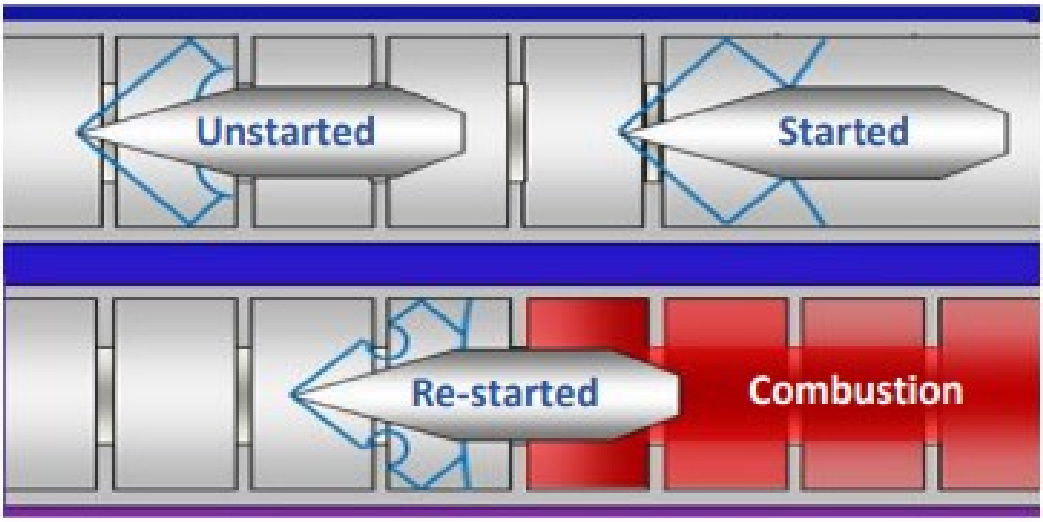

Figure 2.3: Description of the flow field around a projectile as it travels through the BTRA.

The BTRA was devised to overcome three obstacles observed during SBRA ex-

periments. First, the BTRA can utilize propellants that are 2-3 times more energetic than in SBRA by preventing the combustion wave behind the projectile from overtaking the projectile and causing an unstart. Second, the BTRA enables greater muzzle velocities without increasing fill pressure, ensuring propellant densities are reasonable. Third, the BTRA allows for the use of axisymmetric projectiles enabling better operation in the super-detonative velocity regime, which is necessary for applications including direct space launch.[2, 3, 8, 15]

In the BTRA, drag can no longer be neglected on the tube walls and thus must be considered in the thrust equation. BTRA thrust is derived in the same manner as SBRA thrust except for an extra drag term in both the momentum and energy equations, as shown in Eq. 2.11 and Eq. 2.12. Many of the steps involved in the BTRA thrust derivation are identical to the SBRA derivation and will therefore be skipped. Equation 2.13 describes the non-dimensional thrust in a BTRA when baffle drag is considered. Equation 2.14 describes the non-dimensional thrust on the projectile alone. The theoretical models developed later will be compared with non-dimensional projectile thrust.

$$F + D = \left(p_2 A_2 + \rho_2 u_2^2 A_2\right) - \left(p_1 A_1 + \rho_1 u_1^2 A_1\right) \tag{2.11}$$

$$\rho_1 u_1 A_b \left(h_1 + \frac{u_1^2}{2} + \Delta q\right) + D u_1 = \rho_2 u_2 A_b \left(h_2 + \frac{u_2^2}{2}\right) \tag{2.12}$$

$$\begin{aligned} I_{BTRA} &= \frac{F + D}{p_1 A_b} \\ &= M_1(1+\gamma_2)\frac{\gamma_1}{\gamma_2}\sqrt{\left(\frac{\gamma_2 - 1}{\gamma_1 - 1}\right)\left(\frac{\frac{h_1}{c_{p1}T_1} + \frac{\gamma_1 - 1}{2}M_1^2 + Q + \frac{D(\gamma_1 - 1)}{p_1 A_b \gamma_1}}{\frac{h_2}{c_{p2}T_2} + \frac{\gamma_2 - 1}{2}}\right)} \\ &\quad - \left(1 + \gamma_1 M_1^2\right) \end{aligned} \tag{2.13}$$

$$I_{Proj} = I_{BTRA} - \frac{D}{p_1 A_b} \tag{2.14}$$

The energy balance in Eq. 2.12 accounts for work done by baffle drag by adding energy to the control volume just like heat addition. The momentum balance in Eq. 2.11 is written such that thrust and drag are resultant forces acting in the same direction as shown in Fig. 2.4. Here, thrust is the force the projectile exerts on the control volume, and thus the propellants in the tube exert an equal and opposite force on the projectile causing acceleration. This thrust does not produce work in the energy equation because the projectile is stationary in the control volume reference frame, and therefore, thrust does no work to the propellants.[13] The drag, however, is due to pressure forces acting on the baffles that arise from the motion of the combustion products in the laboratory reference frame.

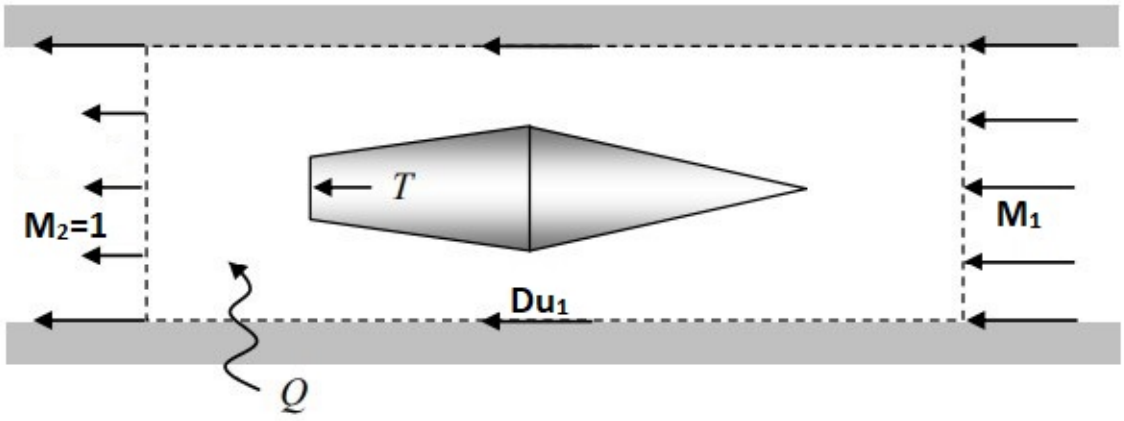

Figure 2.4: Ram accelerator control volume with thrust and drag forces applied.[13]

BTRA thrust can be related to SBRA thrust by equating a baffled tube to a smooth bore tube with an equivalent amount of propellant per unit length, as shown in Fig. 2.5.[14] The equivalent smooth bore tube has an effective area, A_{eff}, which will be larger than the baffle bore area, A_b because of the chamber volumes containing

propellant in the BTRA. The effective area ratio, β, is defined as the ratio of the effective area to the bore area and is calculated in Eq. 2.15, where V_c is the volume of the chamber between baffles, V_b is the volume in the baffle bore, and V_{solid} is the volume of the rails connecting baffles. Other terms include the length of a baffle chamber, L_c, and baffle bore, L_b, as well as the area of the the baffle bore, A_b.

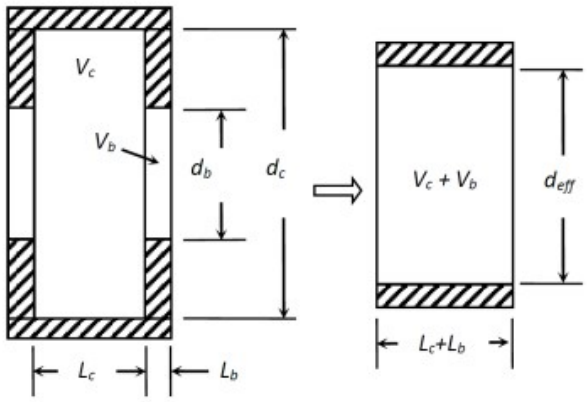

Figure 2.5: The lengths and volumes used to determine β, which relates a baffled tube (left) to a smooth bore tube with an equivalent amount of propellant mass flow over the projectile (right).

$$\beta = \frac{A_{eff}}{A_b} = \frac{V_c + V_b - V_{solid}}{A_b\left(L_c + L_b\right)} \tag{2.15}$$

The effective area ratio stems from the principle of mass conservation and relates BTRA thrust to SBRA thrust as shown in Eq. 2.16. Essentially, β relates the amount of propellant mass flow around a projectile as it passes a baffle insert to the equivalent smooth bore tube that would have the same amount of propellant mass flow around the projectile. A larger β indicates that more propellant is available to accelerate the projectile.[16]

$$I_{BTRA} = \frac{I_{SBRA}}{\beta} = \frac{F}{p_1 A_b}\frac{A_b}{A_{eff}} = \frac{F}{p_1 A_{eff}} \tag{2.16}$$

By solving Eq. 2.16 for the theoretical dimensional thrust, $F = p_1 A_b \beta$, it is clear that more thrust is possible at a given fill pressure for the BTRA than in the SBRA, where $\beta = 1$. Baffled tube experiments in this paper consider an effective area ratio range of $2.217 \leq \beta \leq 2.928$.

2.2 Thermodynamic Parameter Variation

Common simplifying assumptions for control volume analysis are that a gas is calorically perfect, i.e. $\frac{h}{c_p T} = 1$, and that γ has the same value at the inlet and exit state. However, the analysis presented here argues that a calorically perfect assumption does not adequately represent the influence of propellant heat release on the non-dimensional heat release. Further, γ should not be considered constant across the control volume. This analysis utilized a chemical equilibrium code [4] to determine γ and $\frac{h}{c_p T}$ as a function of in-tube Mach number at the control volume inlet and exit planes for a propellant mixture of $1CH_4 + 2O_2 + 4.67N_2$ at 298 K and 20 bar.

Figure 2.6 shows how the caloric imperfection term, $\frac{h}{c_P T}$, and specific heat ratio, γ, change at the control volume exit plane as a function of inlet Mach number. The theoretical performance models in this thesis use $\frac{h_2}{c_{P2} T_2}$ and γ_2 at M_{CJ} to be consistent with using Q_{CJ}.

Equation 2.17 is used to find the non-dimensional heat release at the CJ Mach number as determined by the chemical equilibrum code. This equation is obtained by solving Eq. 2.10 for Q and plugging in the Mach number, γ, and $\frac{h}{c_P T}$ at the CJ speed for a given propellant mixture. Equation 2.17 is solved using the fact that the TCRA produces zero thrust at the CJ speed ($I_{CJ} = 0$), as shown in Fig. 2.2.

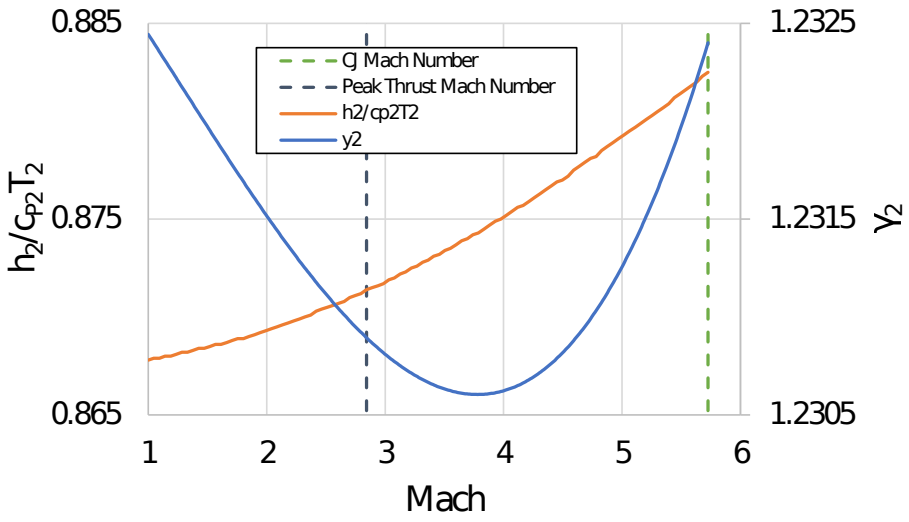

Figure 2.6: Caloric imperfection and specific heat ratio variation with Mach number for a mixture of $1\,CH_4 + 2\,O_2 + 4.67\,N_2$.

$$Q_{CJ} = \left[\frac{\gamma_2\left(1+\gamma_1 M_{CJ}^2\right)}{\gamma_1\left(1+\gamma_2\right)M_{CJ}}\right]^2 \left(\frac{\gamma_1-1}{\gamma_2-1}\right)\left(\frac{h_2}{c_P T_2}+\frac{\gamma_2-1}{2}\right) - \left(\frac{h_1}{c_P T_1}+\frac{\gamma_1-1}{2}M_{CJ}^2\right) \quad (2.17)$$

Table 2.1 below shows the effects of γ and $\frac{h}{c_p T}$ on Q_{CJ}, which is the non-dimensional heat release at the Chapman-Jouguet detonation velocity. The Chapman-Jouguet Mach number represents an upper bound on sub-detonative ($M < M_{CJ}$) ram accelerator operation and is a convenient Mach number to use as a reference for non-dimensional heat release for the TCRA. In Table 2.1, Case 1 shows the "true" non-dimensional heat release at CJ speed when both γ and $\frac{h}{c_p T}$ vary at the control volume inlet and exit as determined by the chemical equilibrium code. In Case 2, neither γ nor $\frac{h}{c_p T}$ vary from inlet to exit, resulting in under-prediction of the "true" Q_{CJ} by nearly 35% from the value in Case 1 (9.6→6.2). In Case 3, only γ varies at inlet and exit while $\frac{h}{c_p T}$ is held constant. Comparing Case 1 to Case 3, there is almost 20%

increase in Q_{CJ} (9.6 $\rightarrow$ 11.4); i.e., an over-prediction of heat release. Finally, in Case 4, only $\frac{h}{c_pT}$ varies at inlet and exit while γ is held constant. Comparing Case 1 to Case 4, Q_{CJ} decreases almost 50% (9.6 $\rightarrow$ 5.0), resulting in an under-prediction of heat release.

Case	γ_1	γ_2	$\frac{h_1}{c_{p1}T_1}$	$\frac{h_2}{c_{p2}T_2}$	Q_{CJ}
1	1.3826	1.2329	0.988	0.882	9.6
2	1.3826	1.3826	0.988	0.988	6.2
3	1.3826	1.2329	0.988	0.988	11.4
4	1.3826	1.3826	0.988	0.882	5.0

Table 2.1: The effect of γ and $\frac{h}{c_pT}$ variation on the prediction of Q_{CJ} for a CJ detonation Mach number of $M_{CJ} = 5.65$ calculated for $1\,CH_4 + 2\,O_2 + 4.67\,N_2$.

The results from Table 2.1 show that in order to properly estimate heat release for a given propellant, it is necessary to consider that the thermodynamic parameters γ and $\frac{h}{c_pT}$ will vary at the control volume inlet plane and exit plane. The decrease in γ leads to an increase in Q_{CJ}, while the decrease in $\frac{h}{c_pT}$ leads to a decrease in Q_{CJ}, albeit less drastic. The caloric imperfection term, $\frac{h}{c_pT}$, effectively acts as a limiter to heat release.

Further, it is clear that assuming propellants behave as calorically perfect gases ($\frac{h}{c_pT} = 1$) within the ram accelerator is a flawed assumption that will lead to misrepresentation of heat release.

Figure 2.7 shows how Q tends to decrease with increasing Mach number when the TCRA thrust is non-zero. This variation is captured by solving Eq. 2.18 for any Mach number using the corresponding zero drag non-dimensional thrust shown in Fig 2.2 and the Mach number dependent thermodynamic parameters. This enables determination of Q using chemical equilibrium codes that do not provide heat release

values based on the difference of enthalpies of formation at 0 K.

$$Q = \left[\frac{\frac{F}{p_1 A_b} + (1 + \gamma_1 M_1^2)}{\frac{\gamma_1}{\gamma_2}(1+\gamma_2) M_1}\right]^2 \left(\frac{\gamma_1 - 1}{\gamma_2 - 1}\right)\left(\frac{h_2}{c_P T_2} + \frac{\gamma_2 - 1}{2}\right) - \left(\frac{h_1}{c_P T_1} + \frac{\gamma_1 - 1}{2} M_1^2\right) \quad (2.18)$$

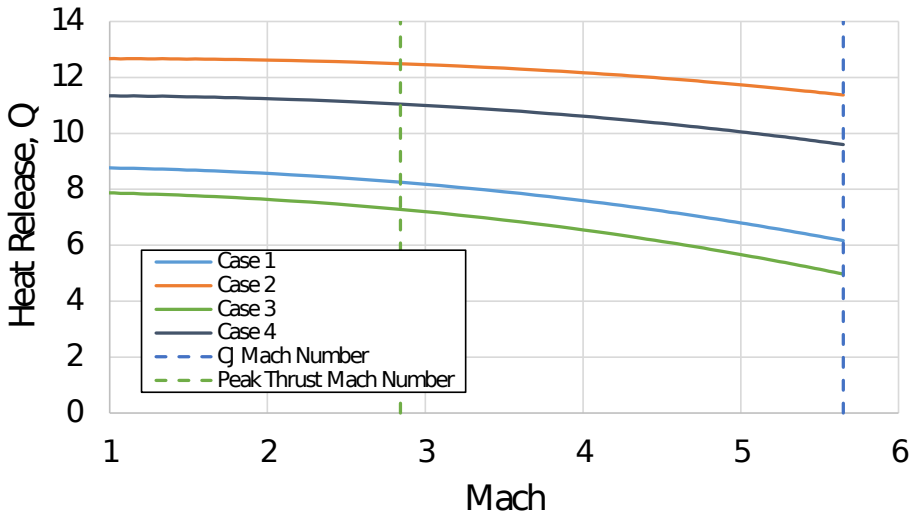

Figure 2.7: Variation of Q with Mach number for the TCRA with a mixture of $1\,CH_4 + 2\,O_2 + 4.67\,N_2$. The specific parameters of each case are listed in Table 2.1

2.3 Combustion Effectiveness

Combustion effectiveness is a concept used to relate the theoretical TCRA heat release to the effective heat release determined empirically. It can be thought of as the ratio of useful heat release to total heat release of a propellant contained in the BTRA. Figure 2.8 shows the control volume used for the derivation of the combustion effectiveness factor, η_c. Baffles are not shown in this control volume for illustration

clarity, but they are considered within the control volume. In Fig. 2.8, the baffle bore, or inner stream tube, is marked in red, while the outer baffle chamber volumes are marked in blue. When combustion occurs in the inner stream tube, the outer chamber volume must be in pressure balance and assumed to absorb heat from combustion, but not contribute to heat release. The result is the net heat release per mass of propellant is reduced by the extra mass of control volume acting as a diluent, which is only a portion of the control volume behind the projectile. The fraction of the control volume length affected can be determined from computational fluid dynamics (CFD) or experimental pressure data and is represented by Ψ.

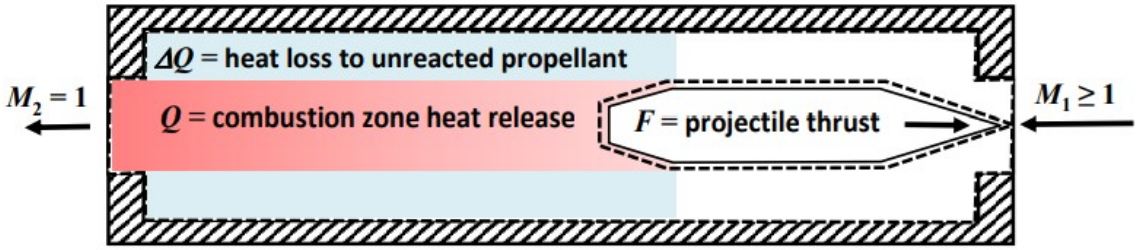

Figure 2.8: The BTRA control volume for combustion effectiveness.

First, it is assumed that the minimum mass flow rate that combusts is the mass flow rate of propellant ingested through the baffle bore; i.e., propellant in the outer chamber volumes does not ignite in time to interact with the projectile. The bore stream tube in Fig. 2.8 has the propellant mass flow rate given below.

$$\dot{m}_b = \rho_1 u_1 A_b = p_1 A_b M_1 \sqrt{\frac{\gamma_1}{R_1 T_1}} = \rho_2 u_2 A_b = p_2 A_b M_1 \sqrt{\frac{\gamma_2}{R_2 T_2}} \tag{2.19}$$

Next, the rate of non-dimensional heat release, $\dot{Q}$, is found by combining Eq. 2.7 with Eq. 2.19. The rate of non-dimensional heat release has the units kg/s, but can be thought of as the chemical power of the propellants in the bore stream tube normalized by reactant properties.

$$\dot{Q} = \dot{m}_b Q = \dot{m}_b \left(\frac{\Delta q}{c_{p1} T_1} \right) \tag{2.20}$$

The mass flow rate in the annulus (blue area in Fig. 2.8) is determined using Eq. 2.21, where $\dot{m}_c$ represents the mass flow rate in the entire chamber.

$$\dot{m}_a = \dot{m}_c - \dot{m}_b \tag{2.21}$$

The corrected heat release, Δq_{eff}, is a fraction of the SBRA heat release based on the portion of the control volume that is unreacted propellant, which can be quantified as the fraction of unreacted propellant in the annular volume of the chamber, Ψ, as shown below.

$$\Delta q_{eff} = \frac{\dot{m}_b \Delta q}{\dot{m}_b + \Psi \dot{m}_a} = \frac{\Delta q}{1 + \Psi \frac{\dot{m}_a}{m_b}} = \frac{\Delta q}{1 + \Psi \left(\frac{\dot{m}_c}{m_b} - 1 \right)} \tag{2.22}$$

Next, the effective non-dimensional heat release is found using Eq. 2.23, where β is substituted for $\frac{\dot{m}_c}{\dot{m}_b}$. As previously mentioned, β relates the mass flow of propellant around a projectile in the baffled tube to the mass flow in a smooth bore tube having the diameter of the baffle bore.

$$Q_{eff} = \frac{\Delta q_{eff}}{c_{p1} T_1} = Q \left(\frac{1}{1 + \Psi \left(\beta - 1 \right)} \right) = \eta_c Q \tag{2.23}$$

Finally, the combustion effectiveness is defined in Eq. 2.24. It was shown earlier that non-dimensional heat release varies with Mach number and mentioned that Q_{CJ} is used as the reference non-dimensional heat release throughout this paper, so that has been denoted.

$$\eta_c = \left(\frac{1}{1 + \Psi \left(\beta - 1 \right)} \right) = \frac{Q_{eff}}{Q_{CJ}} \tag{2.24}$$

Equation 2.13 can now be rewritten using Eq. 2.24 to I_{BTRA} with combustion effectiveness, where Q is now modified by η_c in Eq. 2.14.

$$I_{BTRA} = \frac{F+D}{p_1 A_b}$$
$$= M_1(1+\gamma_2)\frac{\gamma_1}{\gamma_2}\sqrt{\left(\frac{\gamma_2-1}{\gamma_1-1}\right)\left(\frac{\frac{h_1}{c_{p1}T_1}+\frac{\gamma_1-1}{2}M_1^2+\eta_c * Q+\frac{D(\gamma_1-1)}{p_1 A_b \gamma_1}}{\frac{h_2}{c_{p2}T_2}+\frac{\gamma_2-1}{2}}\right)} - \left(1+\gamma_1 M_1^2\right) \quad (2.25)$$

Figures 2.9 and 2.10 can be characterized by a non-dimensional heat release value of $Q_{CJ} = 9.59$, which was determined by solving Eq. 2.17 with $M_{CJ} = 5.65$ for $1\,CH_4 + 2\,O_2 + 4.67\,N_2$ and the combustion product properties at the CJ speed. The unreacted mass fraction, Ψ can be considered the fraction of control volume length affected by propellant not contributing to heat release, so $0 \leq \Psi \leq 1$. The non-dimensional thrust curves from Eq. 2.13 with $D = 0$ plotted in Fig. 2.9 ($\beta = 2.217$) had Ψ varying as a parameter with the corresponding combustion effectiveness indicated in the legend. The theoretical TCRA peak thrust decreases and shifts to lower Mach number while the zero thrust Mach number also decreases with increasing Ψ. Figure 2.10 shows the same trends, but when $\beta = 2.928$. The outer chamber volume grows with β, meaning that the total mass of propellant in the control volume increases while the inner stream tube stays constant. This explains why the thrust curves in Fig. 2.10 are reduced from Fig. 2.9. A tube full of 111 baffles has $\beta = 2.928$ while a tube full of 501 baffles has $\beta = 2.217$. Both baffle types will be discussed in Chapter 3.

Figure 2.11 depicts the effects of Ψ and β on combustion effectiveness, η_c. The combustion effectiveness decreases with increasing Ψ. At a fixed Ψ, the combustion effectiveness decreases with increasing β. For all experiments analyzed in this paper, $2.217 \leq \beta \leq 2.928$.

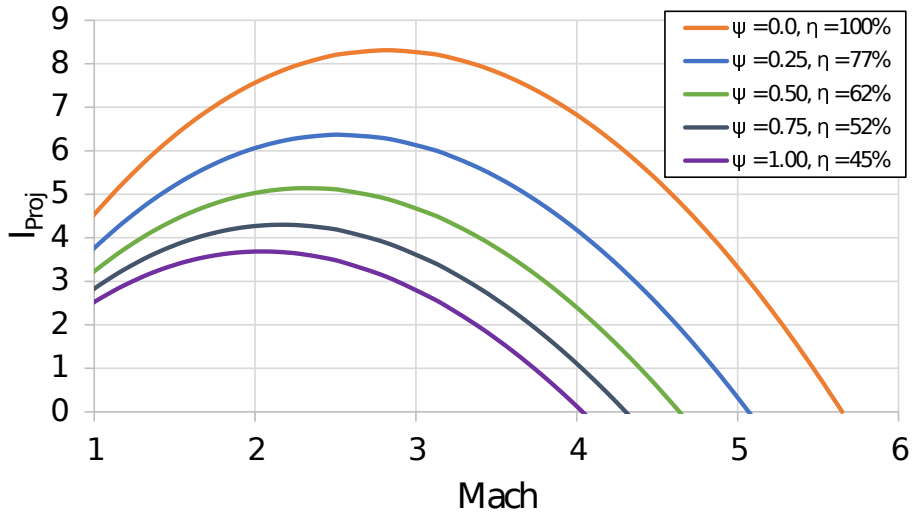

Figure 2.9: Impact of Ψ on theoretical non-dimensional thrust vs. Mach at $\beta = 2.217$. An increase in Ψ means a decrease in combustion effectiveness and a decrease in the thrust.

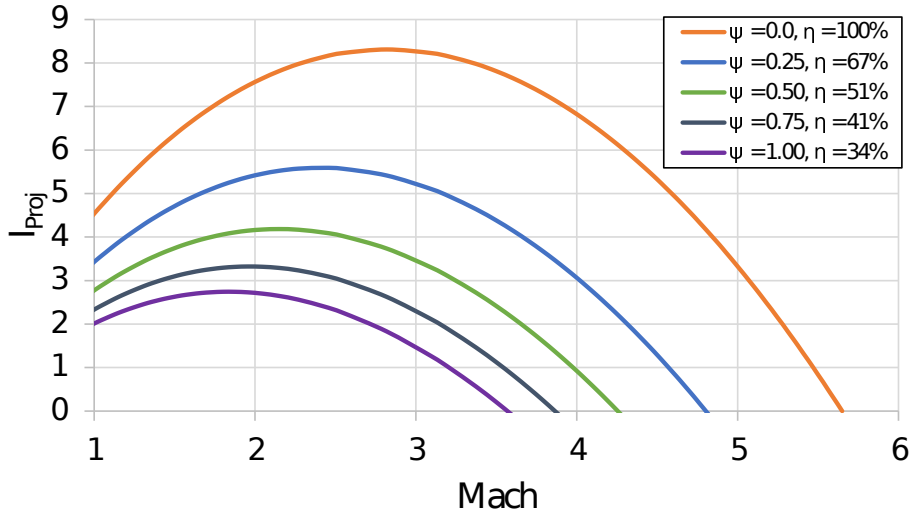

Figure 2.10: Impact of Ψ on theoretical non-dimensional thrust vs. Mach at $\beta = 2.928$. An increase in Ψ means a decrease in combustion effectiveness and a decrease in the thrust.

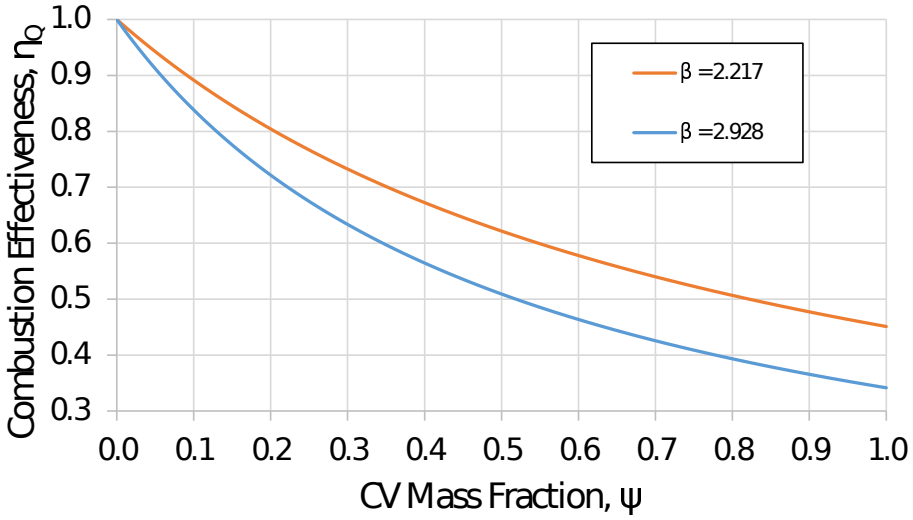

Figure 2.11: Impact of β on combustion effectiveness vs. control volume mass fraction. Combustion effectiveness decreases for larger β.

2.4 Drag Models

In a SBRA, the drag force from friction on the tube walls can be neglected, however, in a BTRA, pressure forces acting on the annular baffle walls provides non-negligible work to the system. The drag models presented here consider the drag experienced by the baffles as propellant is pushed through them. Drag models have previously been developed in [16, 17, 18] with different methods for including drag in the conservation equations as projectile drag and/or baffle drag. Here, the prior drag efforts are reconciled into three drag models consider with the velocity flow in the lab frame of reference.

The drag models differ from one another by the manner in which the lab frame velocity of the propellant that impacts the baffles, $u_1 - u_2'$, is determined behind the projectile. The drag on the baffles is assumed to be proportional to the square of the velocity of the combustion reactants and products in the lab reference frame and the

corresponding density, ρ_2', as shown in Eq. 2.26, where, c_D is the drag coefficient, and $A_c - A_b$ is the area of the baffle annulus.

$$D = \frac{1}{2} c_D \rho_2' |u_1 - u_2'|(u_1 - u_2')(A_c - A_b) \tag{2.26}$$

By using one-dimensional mass conservation, the drag can be expressed in terms of inlet propellant density, ρ_1, as shown in Eq. 2.27. This is the expression used to determine drag as function of Mach number for various assumptions for the lab frame velocity of the propellant impacting the baffles.

$$D = \frac{1}{2} c_D \rho_1 \frac{u_1}{u_2'} |u_1 - u_2'|(u_1 - u_2')(A_c - A_b) \tag{2.27}$$

This formulation of drag allows for negative lab frame velocity when $u_2' > u_1$, which results in negative drag; i.e., drag acting in the opposite direction of projectile motion. The combustion products move at the speed of sound of the thermal choke point relative to the projectile. Therefore, negative lab frame velocity occurs when the sound speed is greater than the projectile velocity, which occurs when operating below the peak thrust Mach number, M_{Imax}. In the scenario of negative lab frame velocity, baffle drag hinders the motion of the combustion products away from the projectile, thereby increasing the pressure on the base of the projectile and acting in the same manner as thrust. [18]

2.4.1 Thermally Choked Plane Drag Model

The thermally choked plane (TCP) drag model is based on the velocity of the combusted propellants at the thermally choked plane, u_2', in the lab frame of reference. The velocity of the combustion products at the TCP are always sonic with respect to the projectile. In the lab frame, however, the products can be subsonic or supersonic in the direction of projectile motion or subsonic in the opposite direction.

The theoretical non-dimensional thrust on the projectile vs. Mach number is

plotted in Fig. 2.12 with the drag coefficient ranging from $0 \leq c_D \leq 1$. The thrust is augmented by drag at Mach numbers below M_{Imax}. This is because the combustion products move in the opposite direction of the projectile below M_{Imax}, resulting in negative drag. The products at the TCP have zero velocity at M_{Imax}, and then move in the same direction as the projectile at higher Mach numbers. To the right of M_{Imax}, baffle drag has a more expected influence; i.e., decreasing projectile thrust more extensively as Mach number increases. In the TCP drag model, all curves pass through $M_{Imax}|_{c_D=0}$, but not all curves exhibit the same M_{Imax}.

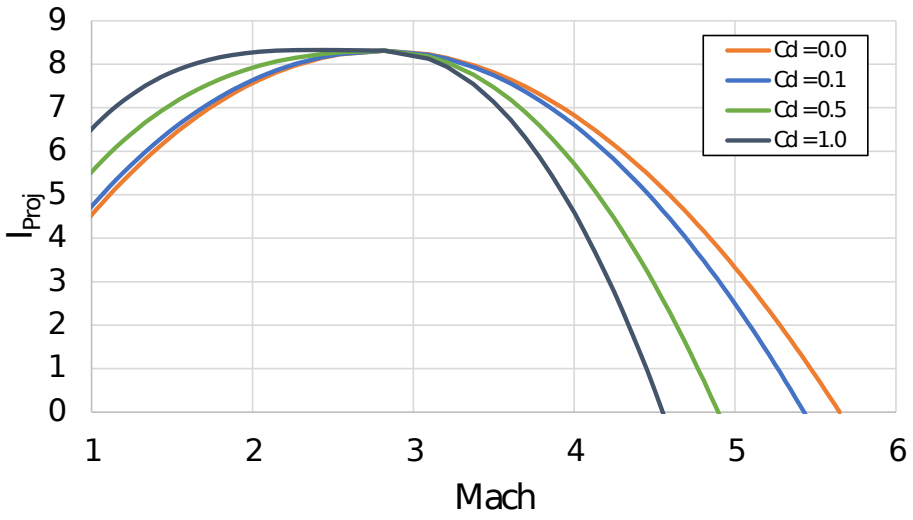

Figure 2.12: The thermally choked plane drag model for any β when $\Psi = 0$ and $0 \leq c_D \leq 1$.

2.4.2 Normal Shock Drag Model

The normal shock (NS) drag model is based on the lab frame velocity of the uncombusted propellants on the downstream side of the normal shock wave just behind the projectile that travels at the speed of the projectile, u_2'. This assumes the flow is supersonic over the projectile for the purposes of estimating the influence of in-tube

Mach number of the drag force generated by shock compressed flow on the baffles. The velocity downstream of the normal shock wave will always be $u_2' \leq u_1$, meaning that negative drag is not observed in the NS drag model.

The influence of the NS drag model on I_{Proj} with 100% combustion effectiveness is plotted with the c_D ranging from 0 to 1 in Fig. 2.13, which shows the NS drag model is much more sensitive to drag coefficient than the TCP drag model. Since $(u_1 - u_2') \geq 0$, drag always acts in the direction of projectile motion. It is evident that both M_{Imax} and I_{max}, decrease as drag increases in the NS drag model. The zero thrust Mach number also decreases with increasing drag.

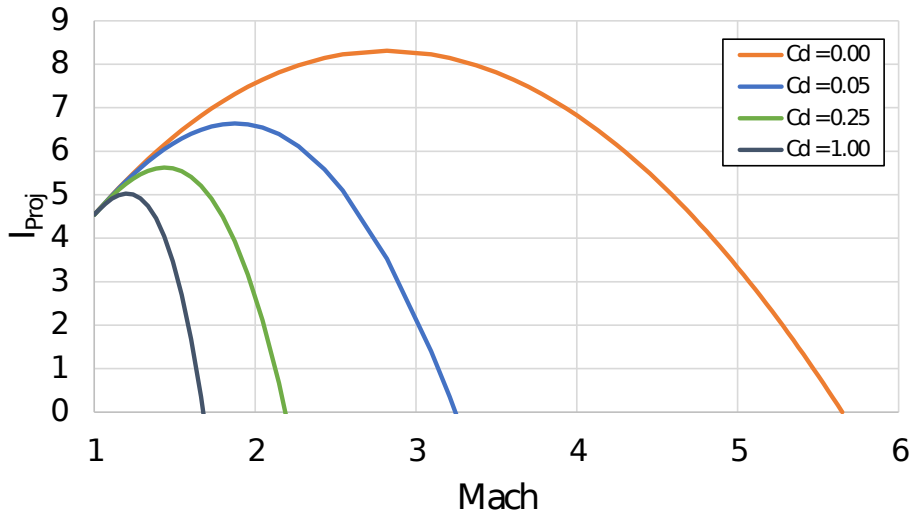

Figure 2.13: The normal shock drag model for any β when $\Psi = 0$ and $0 \leq c_D \leq 1$.

2.4.3 TCP-NS Average Drag Model

The TCP-NS Average (AVG) drag model serves to capture the effects of both the TCP and NS drag models. Negative drag is possible at low Mach numbers and so is a reduction in M_{Imax} due to drag. The AVG drag model is calculated by averaging the

u_2' velocities from the TCP and NS drag at any given Mach number. The resulting drag force is used in Eq. 2.13 to find I_{BTRA}, just as with the two previous models.

Figure 2.14 shows that a much smaller amount of thrust is produced from drag below M_{Imax} than the TCP model. This is because of negative lab frame velocity as mentioned earlier. Similar to the TCP model, negative drag acts to increase thrust below M_{Imax} and then opposes thrust above M_{Imax}. In addition to this effect, the NS drag model's tendency to decrease M_{Imax} also appears.

In the AVG drag model, M_{Imax} decreases with increasing drag and I_{max} ranges from $2 \leq M \leq 2.8$. With increasing c_D, the zero thrust Mach number decreases more than predicted from the TCP drag model and less than the NS drag model.

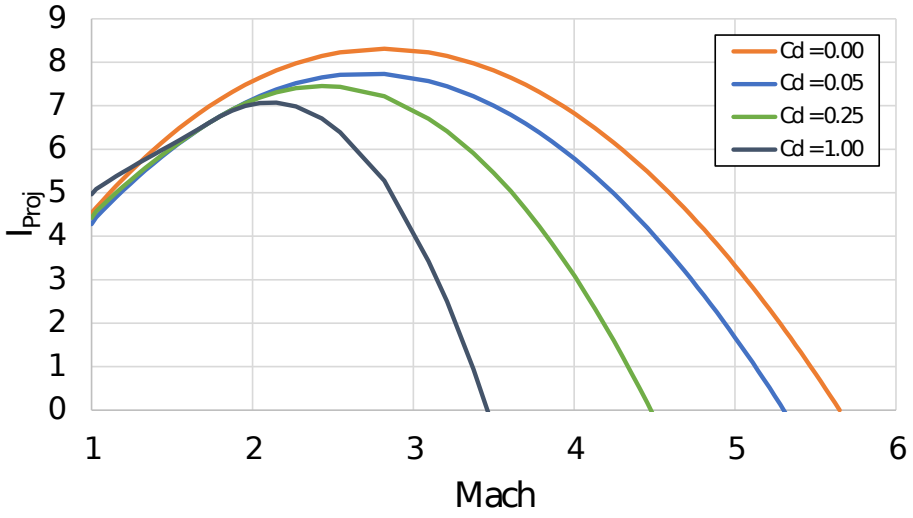

Figure 2.14: The average drag model for any β when $\Psi = 0$ and $0 \leq c_D \leq 1$.

Finally, all three drag models are shown together in Fig. 2.15 at $c_D = 1$. The drag force grows significantly faster with NS drag than with TCP drag, so it dominates the average curve, particularly at higher drag coefficients. The baffle drag influence on thrust below M_{Imax} is exhibited but is not as significant for the AVG drag model as it is with the TCP drag model.

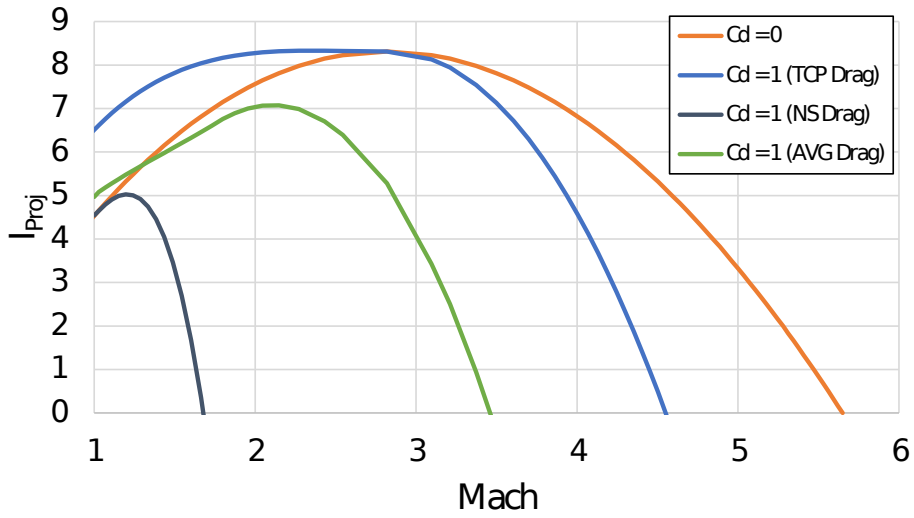

Figure 2.15: Comparison of all three drag models for any β with $\Psi = 0$ at $C_d = 0$ and $C_d = 1$.

Chapter 3
EXPERIMENTAL FACILITY AND METHODS

Detailed in this chapter is the UW ram accelerator facility, including the 8-m experimental setup used to collect the data analyzed in Chapter 4. All experiments were performed with the BTRA, but they made use of several different baffle types and configurations as well as multiple projectiles that varied in length, material, and density.

3.1 Experimental Apparatus

The UW ram accelerator consists of three main sections: a single stage light gas gun, the ram accelerator test section, and a decelerating section consisting of a dump tank and catcher tube. A schematic of the ram accelerator experiment is shown in Fig. 3.1

The single stage helium light gas gun is used to accelerate projectiles up to the speeds required to initiate the ram accelerator's propulsive cycle. The light gas gun is 6-m in length with a 38-mm bore and can accelerate projectiles up to 1.2 km/s.[14] A dump tank is used to vent helium from the launch tubes before the projectile enters the ram accelerator test section.

The ram accelerator launcher consists of eight 2-m tubes connected in series to form a 16-meter test section. Two test section configurations were used to collect the data analyzed in this paper. The first included 4-m of baffled tube and 12-m of smooth bore tube, while the second involved 8-m of baffle tube and 8-m of smooth bore tube. Two-meter-long shell tubes contain 56 baffle inserts with each having a 38-mm bore and 76-mm outer diameter. Mylar diaphragms are used to isolate the test section and can be used to isolate each 2-m tube for staging of different propellant

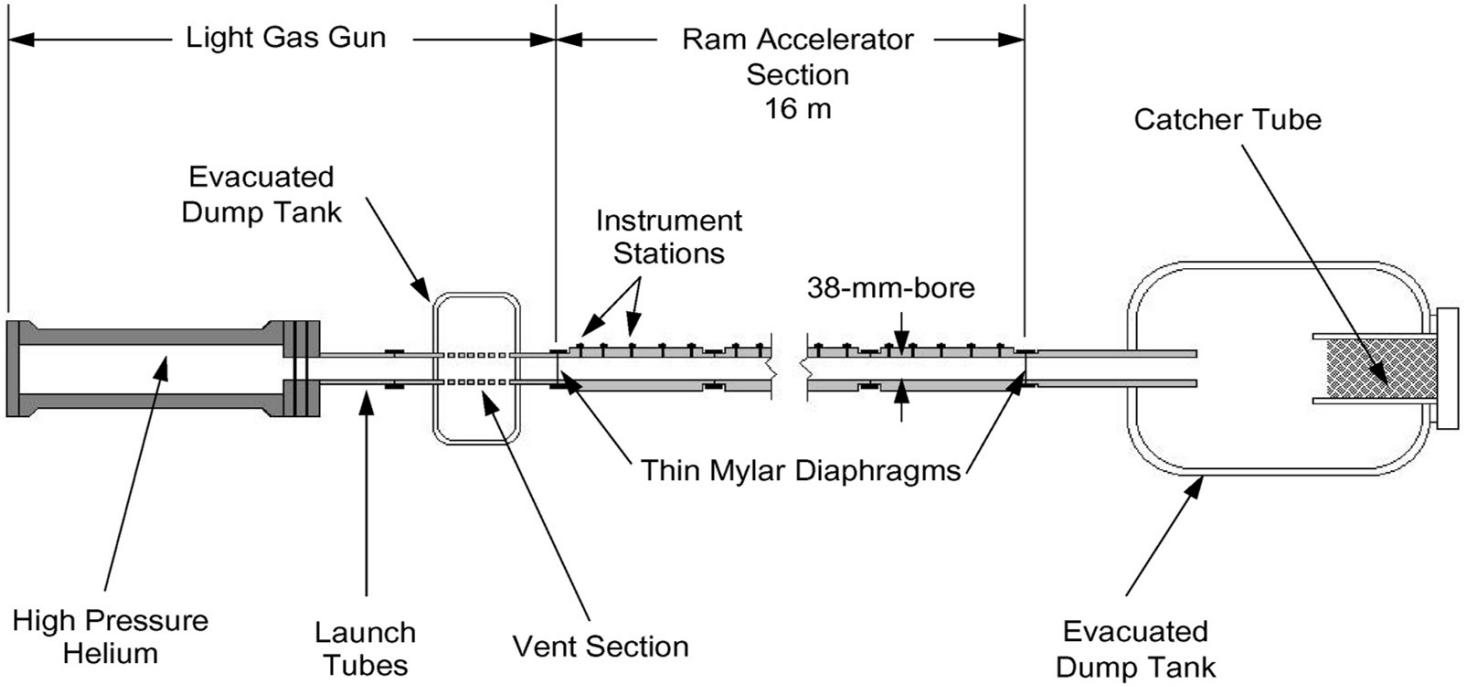

Figure 3.1: Schematic of the ram accelerator experimental apparatus.

or fill pressures. Each 2-m tube has five instrument stations consisting of a pair of instrument ports 180 degrees from each other. Instrumentation includes piezoelectric pressure transducers (PCB119) and in-house built electromagnetic (EM) probes.[19] Propellants are mixed by co-flowing into the test section using mass flow controllers to regulate stoichiometry. A more detailed overview of the gas handling system is presented in [20].

The decelerator section begins with a dump tank that captures the combustion products from the test section. The projectile flies freely through the dump tank until reaching the catcher tube, which is filled with tightly packed carpet to halt projectile motion.

Experimental data is sampled at 1.25 MHz over 32 analogue input channels with a National Instruments PXIe-1071 chassis with two PXIe-6358 modules. Up to 40 EM signals are routed through multiplexers to 6 of the analogue channels, leaving 26 channels for pressure transducers and other instrumentation. The pressure transducers measure tube wall pressure, while the EM probes track a neodymium magnet inside of projectiles to determine time-of-passage and projectile velocity with known distances between instrument stations. The velocity-distance data is used to determine non-dimensional thrust-Mach data that will be analyzed in Chapter 4.

Due to the relatively large distance from shell tube centerline to its inner wall (38 mm) and the signal distortion that arises from the internal baffle geometry, it is sometimes difficult to acquire time-of-passage data with low uncertainty from the EM sensors in the BTRA. Thus, the experimental thrust measurements are based on the entrance and exit velocities measured in each of the 2-m long tubes.[18] The uncertainty in average velocity and acceleration in each 2-m-long tube due to 1.25 MHz sampling rate, sensor position precision, and signal distortion is estimated to be +/-15 m/s (1.5%) and +/-225 m/s2 (3%), respectively.

3.2 Projectiles

Figure 3.2 shows the axisymmetric projectile design used for these experiments. Projectiles were one-piece construction made from either polycarbonate or aluminum alloy. The projectile's shoulder diameter was 35.1-mm while shoulder length varied from 59.1-mm to 179-mm. The diametric clearance of the shoulder and baffle bore was 3 mm, which has proven to be effective over a wide range of test conditions. A threaded nylon plug retained a neodymium magnet inserted in the projectile base. An obturator with diameter of 37.4-mm prevented blow-by during the light gas gun launch and facilitated ignition of the propellant during the starting process. Projectiles fabricated from polycarbonate ranged from 175-g to 260-g. Aluminum projectiles were roughly 265-g and the obturators used were roughly 23-g.[14]

Advantages of axisymmetric projectiles, which the BTRA enables, is that they are easier to machine and provide greater volume-to-surface ratio for more payload capacity. All projectiles tested had a nose cone half-angle of 15°, a tail half-angle of 12°, cylindrical shoulder diameter of 35.1-mm (1.38-in), base diameter of 18-mm, and total length dependent on the length the shoulder region. A machine drawing for the single-piece projectile is shown in Fig. 3.2.[9]

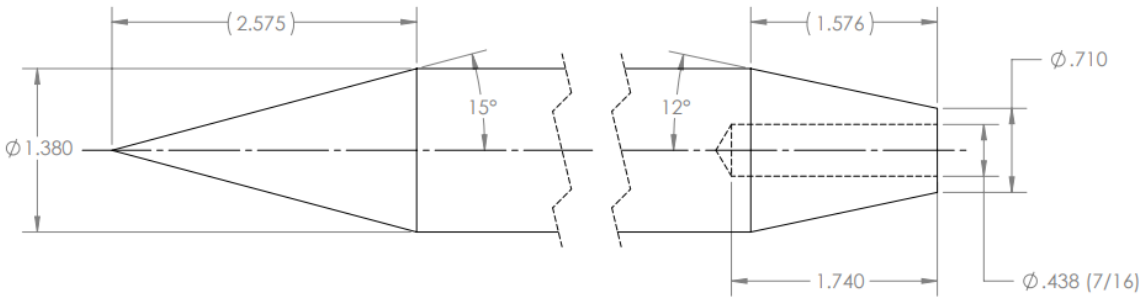

Figure 3.2: A P380 projectile of arbitrary shoulder length (dimensions in inches).

Three projectiles of different lengths were tested during experiments. A 1.7 baf-

fle length (BL) projectile, a 3BL projectile, and a 5BL projectile, corresponding to 59.1-mm, 107-mm, and 179-mm, respectively. Figure 3.3 shows each of the different projectiles. The 1.7BL projectile was made of aluminum alloy, while the 3BL and 5BL projectiles were polycarbonate.

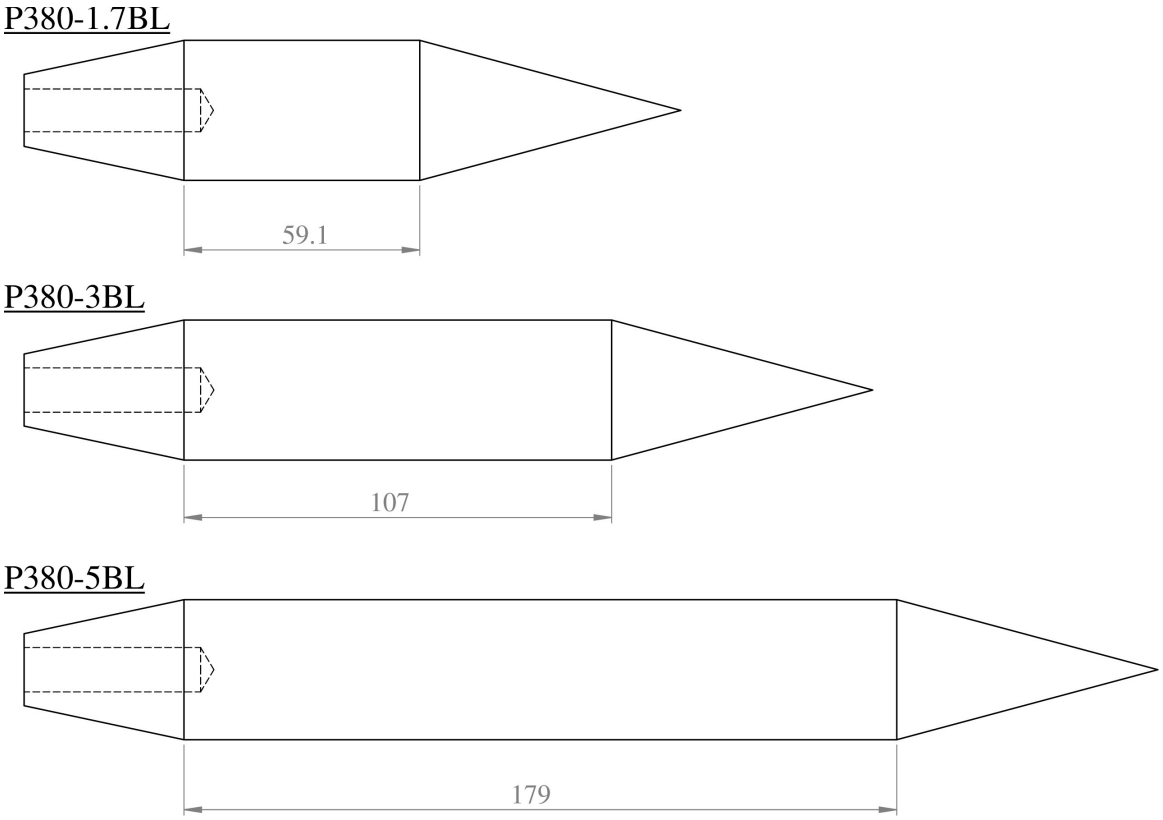

Figure 3.3: A P380 projectile with 1.7, 3, and 5 baffle length shoulders. The nose and tail-cone geometry is identical for each.

3.3 Baffle Inserts

The three different baffle inserts used during experiments are shown in Fig. 3.4. Each 2-m tube in the ram test section contains 56 baffle inserts, which all have the same length (35.8-mm), but vary in geometry. A full 2-m baffled tube containing only 501,

501s, or 111 baffles will have $\beta = 2.217$, $\beta = 2.223$, or $\beta = 2.928$, respectively.

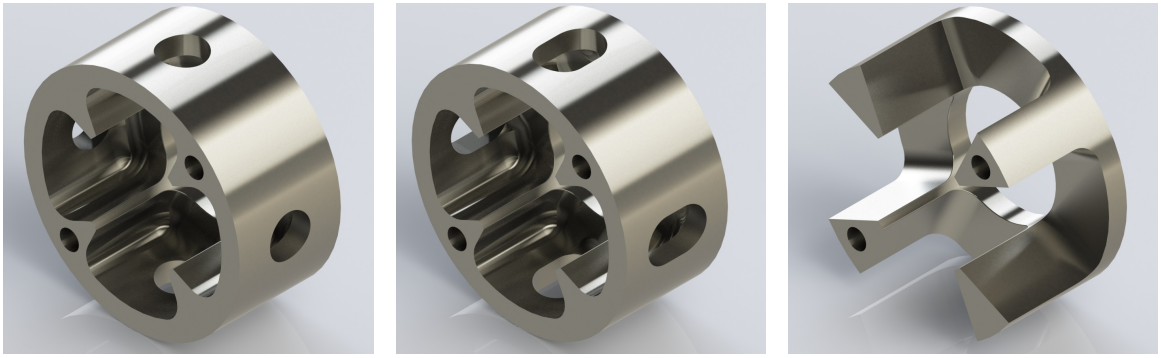

Figure 3.4: The 501 (left), 501s (middle), and 111 (right) baffle designs.

Three baffle configurations (BC) were used in the 8-m experiments analyzed in this paper. The first configuration's baffled tube (BT) 1 consisted completely of 111 baffles, while the remaining three tubes, BT 2, BT 3, and BT 4, contained a mix of 501 and 501s baffles. The second configuration simply swaps BT 1 and BT 2 from baffle configuration 1, while keeping BT 3 and BT 4 the same. The third configuration focused on placing 111 baffles in BT 1 and at each instrument station within all four baffled tubes. Table 3.1 specifies which baffles were used in which baffled tube for the range of hot shots analyzed in this paper. The corresponding β factor for each baffled tube is shown in Table 3.2.

BC No.	HS No.	BT 1	BT 2	BT 3	BT 4
1	2271 - 2272	111	501	501	501s
2	2273 - 2297	111	501 & 501s	501 & 501s	501 & 501s
3	2298 - 2302	501 & 501s	111	501 & 501s	501 & 501s
4	2303 - 2312	111 & 501	501 & 111	501 & 111	501 & 501s & 111

Table 3.1: Four different baffle configurations were used during the 8-m experiments.

BC No.	HS No.	β BT 1	β BT 2	β BT 3	β BT 4
1	2271 - 2272	2.928	2.217	2.217	2.280
2	2273 - 2297	2.928	2.223	2.223	2.258
3	2298 - 2302	2.223	2.928	2.223	2.258
4	2303 - 2312	2.889	2.371	2.370	2.418

Table 3.2: The β values for each of the four baffle configurations used during 8-m experiments.

Chapter 4
RESULTS AND DISCUSSION

This chapter focuses on applying the theoretical models to experimental data to examine agreement. Three test series were analyzed for the comparison including a variation of baffle configuration, projectile length, and equivalence ratio. When comparing performance models with drag against experimental data, the average drag model will be used because it captures the effects of both the TCP drag and the NS drag.

4.1 Baffle Configuration

For this comparison, 8-m ram accelerator experiments using P380-3BL projectiles and a mixture of $1\,CH_4 + 2\,O_2 + 4.67\,N_2$ were sorted into two categories based on the average effective area ratio, β, of the test section configuration. Figure 4.1 compares performance models and experimental data for $\beta = 2.928$ and $\beta = 2.235$.

The theoretical non-dimensional projectile thrust profiles plotted in Fig. 4.1 without drag were tuned to the experimental results by adjusting only the combustion effectiveness, η_c. Assuming the combustion of only the propellant within the bore stream tube was contributing to thrust such that $\eta_c = 34\%$ ($\Psi = 1$) resulted in good agreement for the 111 baffle data ($\beta = 2.928$). For the smaller chambers of the 501 baffles ($\beta = 2.235$), $\eta_c = 47\%$ ($\Psi = 0.9$) best matched the experimental data, which implies more of the propellant was combusting in a manner that contributed to projectile thrust. The 111 baffles trap more propellant in their outer chamber volume than 500 series baffles, so it follows that 111 baffles exhibit less combustion effectiveness.

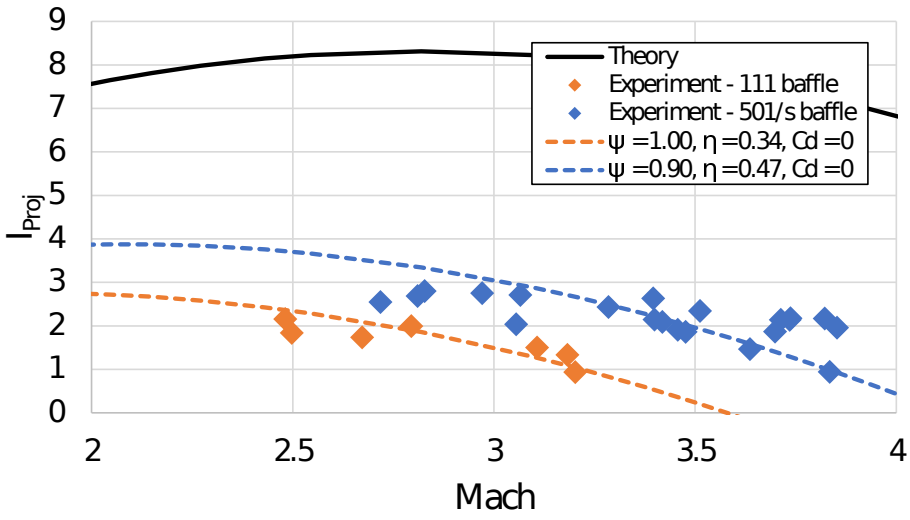

Figure 4.1: P380-3BL projectile with $1\,CH_4 + 2\,O_2 + 4.67\,N_2$ mixture. The beta values for the 111 and 500 series baffle inserts were $\beta = 2.928$ and $\beta = 2.235$, respectively.

4.2 Body Length

Figure 4.2 compares performance models for P380 aluminum alloy and polycarbonate projectiles with lengths: 1.7BL, 3BL, and 5BL. The aluminum alloy projectile was 1.7BL while the 3BL and 5BL projectiles were polycarbonate. Since all experiments were performed in the same baffle configuration, the baffle drag coefficient for the average drag model was kept constant and only combustion effectiveness was tuned. The drag coefficient ($c_D = 0.2$) was decided by first tuning the performance model to the 5BL experimental data, and then leaving c_D unchanged for 1.7BL and 3BL projectiles in an attempt to determine how baffle drag accounts for the differences in thrust. The fractions of the annular volume of propellant not contributing to thrust for the 5BL and 1.7BL projectiles were reduced from $\eta_c = 100\%$ ($\Psi = 0$) to $\eta_c = 59\%$ ($\Psi = 0.5$) and $\eta_c = 47\%$ ($\Psi = 0.8$), respectively, to have theory more closely agree with the experimental results. All body length experiments shown used 500 series

baffles ($\beta = 2.235$).

To match the 3BL experimental thrust at $M_1 = 3.4$, the annular mass fraction not contributing to thrust was reduced $\eta_c = 100\%$ ($\Psi = 0$) to $\eta_c = 64\%$ ($\Psi = 0.4$). The slope of this theoretical thrust-Mach curve, while assuming the same baffle drag coefficient ($c_D = 0.2$), was steeper than that of the 3BL experimental data. The 3BL thrust curve shown has higher combustion effectiveness than both the 1.7BL and the 5BL, which might suggest that there is a middle "sweetspot" in terms of projectile length. It is possible that projectile body length plays a role in combustion effectiveness and maybe should be incorporated in the model. Longer projectiles may give propellants more time to combust and still have an effect on projectile thrust. When the combustion has more time to occur, more heat is released in the immediate vicinity of the projectile, thereby raising pressure and providing more thrust.

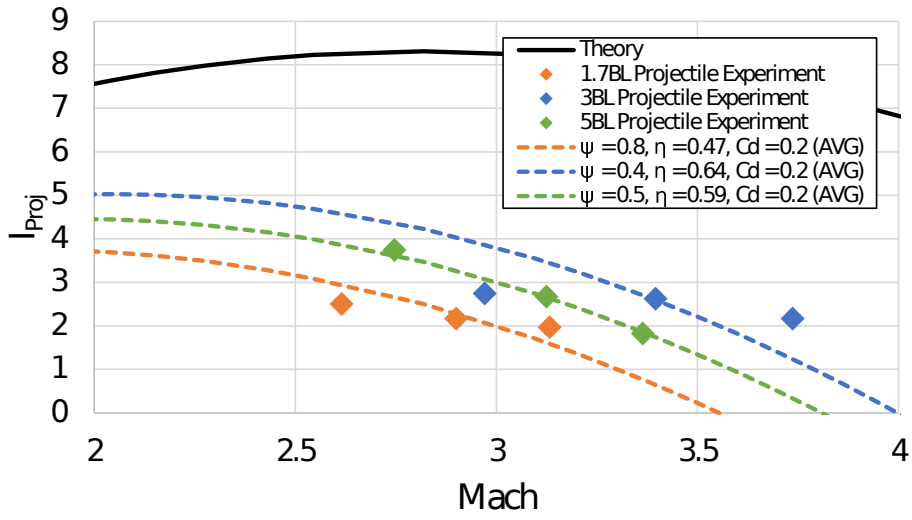

Figure 4.2: P380 polycarbonate projectiles with $1\,CH_4 + 2\,O_2 + 4.67\,N_2$ mixture. The average drag model is plotted against experiments for three different lengths of projectiles. $c_D = 0.2$ for each curve, while Ψ was allowed to vary. The average $\beta = 2.235$.

4.3 Equivalence ratio

Figure 4.3 compares theoretical models will experimental results for P380-1.7BL-Al (aluminum alloy) projectiles in four different equivalence ratios for 500 series baffles ($\beta = 2.235$). The stoichiometric mixture ratio for 30% oxygen-enriched methane-air is $1\,CH_4 + 2\,O_2 + 4.67\,N_2$. Increasing equivalence ratio increases the ratio of methane to all other reactants, which then acts as diluent. Similar to the models in Fig. 4.2, it was intended to set c_D to the value that agreed best with $\phi = 1$ and leave it constant for all other ϕ while adjusting combustion effectiveness.

The fractions of the annular volume of propellant not contributing to thrust for each equivalence ratio were reduced from 100% ($\Psi = 0$) to 0% ($\Psi = 1$) and left constant for all cases to investigate how well combustion effectiveness might translate between equivalence ratio variations. With a theory curve in Fig. 4.3 for each equivalence ratio, a constant Ψ and c_D among $1.0 \leq \phi \leq 1.6$ would have supported the fidelity of the model. The best agreement for $\phi = 1, 1.2$ was with $\eta_c = 45\%$ ($\Psi = 1.0$) and $c_D = 0.15$. At $\phi = 1.4, 1.6$, it became clear that $c_D = 0.15$ was not enough drag to shift the theory curve in line with experimental results. Drag coefficient was then set to best agree with the $\phi = 1.6$ data at $c_D = 0.45$ and kept at the same value for $\phi = 1.4$.

Similarly, Fig. 4.4 shows the P380-1.7BL-Al in the same four equivalence ratios with 111 baffles ($\beta = 2.928$). Combustion effectiveness was reduced from from 100% ($\Psi = 0$) to 0% ($\Psi = 1$), and then the drag coefficient was adjusted for agreement between the model and the $\phi = 1$ experiment ($c_D = 0.65$). This drag coefficient was not sufficient to show agreement when $\phi = 1.4, 1.6$, so drag coefficient was increased to $c_D = 1$ for better agreement with $\phi = 1.6$. Similar to Fig. 4.3, the best agreement was for $\phi = 1, 1.2$ when $\eta_c = 34\%$ ($\Psi = 1.0$) and $c_D = 0.65$.

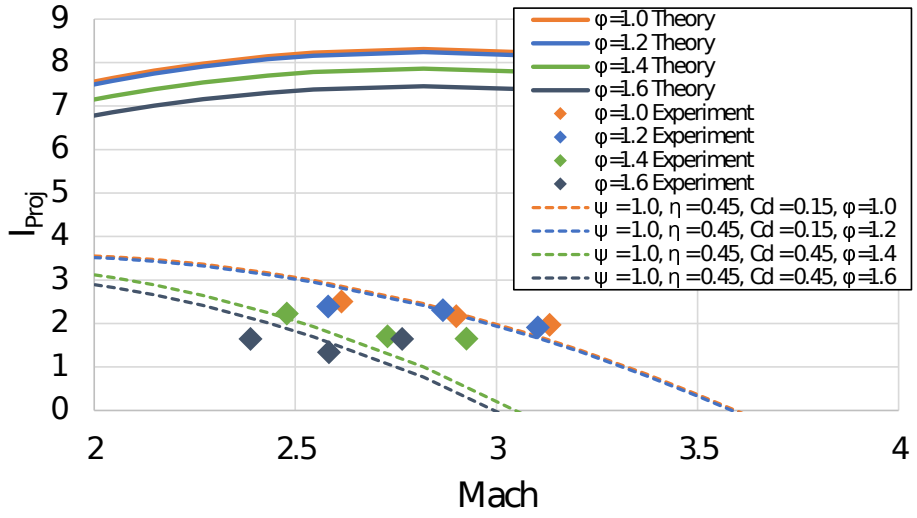

Figure 4.3: P380-1.7BL AL projectile in 500 series baffles with varying equivalence ratios for a mixture of $1\,CH_4 + 2\,O_2 + 4.67\,N_2$. $\Psi = 1.0$. The average $\beta = 2.235$.

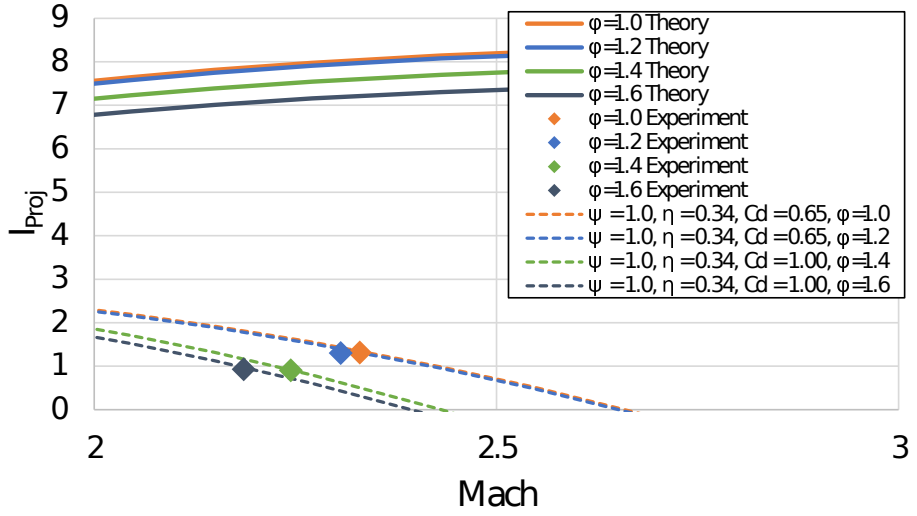

Figure 4.4: P380-1.7BL AL projectile in 111 baffles with varying equivalence ratios for a mixture of $1\,CH_4 + 2\,O_2 + 4.67\,N_2$. $\Psi = 1$. $\beta = 2.928$.

4.4 Combustion Effectiveness and Drag Models

In each of the theoretical performance models developed, the combustion effectiveness tends to be between $0.35 \leq \eta_c \leq 0.65$, meaning only 35-65% of the energy added from combustion is contributing to thrust on the projectile. The baffles appear to trap propellant in the outer chamber volumes, which does not combust in time to raise the pressure on the base of the projectile. Tuning the fraction of the annular volume of propellant not contributing to thrust, Ψ, to adjust combustion effectiveness appeared to be the best solution for tuning the performance models to agree with experimental data. By altering Ψ, the models showed the ability to predict similar peak thrust and thrust vs. Mach as the experimental data showed.

The average drag model does well capturing the effects of both the TCP drag model and the NS drag model. Figures 4.1 - 4.4 show that drag coefficient changes significantly using the theoretical models developed. Sometimes, the model agrees with experiment best when $c_D = 0$ and other times when $c_D = 1$.

Chapter 5

CONCLUSIONS

5.1 Conclusion

The influences on the non-dimensional thrust predicted by the one-dimensional model for the thermally choked ram accelerator propulsive mode due to three different drag models and the use of a combustion effectiveness parameter were investigated. The physical reasoning behind each of these models was discussed and their individual impacts on the theoretical thrust were shown. A chemical equilibrium code was used to calculate the Mach number dependent non-dimensional thrust and the thermodynamic properties of the combustion products.

One of the key findings from this analysis is that propellants are calorically imperfect in the ram accelerator. Also, the difference in caloric imperfection and gamma for combustion products and reactants is crucial in accurately calculating non-dimensional heat release of a propellant. Further, of the theoretical models proposed, combustion effectiveness shows stronger agreement with experimental trends. Combustion effectiveness does well to bring BTRA theory to similar thrust levels as those shown experimentally, and can serve as the primary model tuning mechanism. Finally, the average drag model was useful in modeling experiments because it incorporates the effects of both the thermally choked plane (TCP) drag model and the normal shock (NS) drag model; i.e., drag still contributes to thrust at low Mach numbers (like TCP) while having less steep thrust curves and less influential drag at higher Mach numbers (like NS).

5.2 Prospectus

Directions for future work to support model development BTRA experimental operation over a wider range of Mach numbers. Low Mach number operation is limited by the starting speeds required, but might show whether baffle drag contributes to projectile thrust at low Mach numbers, like the TCP drag model suggest. High Mach number operation will help discern whether the zero thrust Mach number predicted by the models is accurate, or if it is under-predicted. Both outcomes would lead to further development of the performance models.

Finally, an adjustment to the chemical equilibrium code so that it calculates non-dimensional heat release with reference to 0 K and outputs the result as a function of Mach number would be an improvement over the current calculation process.

BIBLIOGRAPHY

[1] N. Daneshvaran and C. Knowlen, "Transient Computational Fluid Dynamic Modeling of Baffled Tube Ram Accelerator," *AIAA SciTech Forum*, Grapevine, TX, 2017. https://doi.org/10.2514/6.2017-0119.

[2] A. Bruckner and C. Knowlen, "Direct Space Launch Using Ram Accelerator Technology," *Space Technology and Applications International Forum*, Albuquerque, NM, 2001. https://doi.org/10.1063/1.1357980.

[3] C. Knowlen, B. Joseph, and A. Bruckner, "Ram Accelerator as an Impulsive Space Launcher: Assessment of Technical Risks," *26th International Space Development Conference*, Dallas, TX, 2007.

[4] A. Bruckner, C. Knowlen, A. Hertzberg, and D. Bogdanoff, "Operational Characteristics of the Thermally Choked Ram Accelerator," *Journal of Propulsion and Power, Vol. 7, No. 5*, 1991. https://doi.org/10.2514/3.23398.

[5] T. Elder and M. Russell, "Design and Operation of a 12.7-mm-bore Railed-Tube Ram Accelerator," *AIAA Region VI Student Conference*, Seattle, WA 2012.

[6] D. Kruczynski, A. Horst, and T. Minor, "Experimental Demonstration of a 120-mm Ram Accelerator," *Army Research Laboratory, Aberdeen Proving Ground*, Aberdeen, MD, 1996.

[7] A. Hertzberg, A. Bruckner, and D. Bogdanoff, "Ram Accelerator: A New Chemical Method for Accelerating Projectiles to Ultrahigh Velocities," *AIAA Journal, Vol. 26, No. 2*, 1988. https://doi.org/10.2514/3.9872.

[8] A. Higgins, C. Knowlen, and C. Kiyanda, "Gasdynamics Operation of Baffled Tube Ram Accelerator in Highly Energetic Mixtures," *19th International Colloquium on the Dynamics of Explosions and Reactive Systems*, Montreal, Canada, 2005.

[9] C. Knowlen, J. Glusman, R. Grist, A. Bruckner, and A. Higgins, "Experimental Investigation of a Baffled-Tube Ram Accelerator," *AIAA/SAE/ASEE Joint Propulsion Conference*, Salt Lake City, UT, 2016. https://doi.org/10.2514/6.2016-4813.

[10] A. Hertzberg, A. Bruckner, and C. Knowlen, "Experimental Investigation of Ram Accelerator Propulsion Modes," *Shock Waves, Vol. 1, No. 1*, 1991.

[11] C. Knowlen and A. Bruckner, "A Hugoniot Analysis of the Ram Accelerator," *18th International Symposium on Shock Waves*, Sendai, Japan, 1991. https://doi.org/10.1007/978-3-642-77648-9_97.

[12] C. Knowlen, "Theoretical and Experimental Investigation of the Thermodynamics of the Thermally Choked Ram Accelerator," *Ph.D. Thesis*, William E. Boeing Department of Aeronautics and Astronautics, University of Washington, Seattle, WA, 1991.

[13] V. Tanguay and A. Higgins, "On the Inclusion of Frictional Work in Non-Ideal Detonations," *19th International Colloquium on the Dynamics of Explosions and Reactive Systems*, Montreal, Canada, 2005.

[14] C. Knowlen, B. Leege, J. Correy, C. Smith, and A. Higgins, "Baffled-Tube Ram Accelerator Operation with Methane-Air Propellant," *28th International Colloquium on the Dynamics of Explosions and Reactive Systems*, Naples, Italy, 2022. https://doi.org/10.2514/6.2022-2071.

[15] A. Higgins, "Ram Accelerators: Outstanding Issues and New Directions," *Journal of Propulsion and Power, Vol. 22, No. 6*, 2006. https://doi.org/10.2514/1.18209.

[16] J. Glusman, "Theoretical Performance Model and Initial Experimentation of a Baffled-Tube Ram Accelerator," *Master's Thesis*, William E. Boeing Department of Aeronautics and Astronautics, University of Washington, Seattle, WA, 2016.

[17] T. Byrd, "Experimentally-Driven Model for the Baffled-Tube Ram Accelerator," *Master's Thesis*, William E. Boeing Department of Aeronautics and Astronautics, University of Washington, Seattle, WA, 2018.

[18] C. Knowlen, N. Daneshvaran, T. Byrd, and J. Dumas, "Computational Fluid Dynamic Modeling of Baffled Tube Ram Accelerator Experiments," *AIAA SciTech Forum*, Kissimmee, FL, 2018. https://doi.org/10.2514/6.2018-1417.

[19] D. W. Bogdanoff, C. Knowlen, D. Murakami, and I. Stonich, "Magnetic Detection for Projectiles in Tubes," *AIAA Journal, Vol. 28, No. 11*, 1990. https://doi.org/10.2514/3.10502.

[20] C. Knowlen, C. Bundy, R. Schwab, and A. Bruckner, "High Pressure Ram Accelerator Facility," *50th Meeting of the Aeroballistic Range Association*, 1999.

[21] S. Depraz, C. Knowlen, P. Bauer, and A. Higgins, "New Tools for Ram Accelerator Performance Modeling," *21st International Colloquium on the Dynamics of Explosions and Reactive Systems*, Poiters, France, 2007.

Appendix A

BAFFLED TUBE RAM ACCELERATOR SHOT LOG

Baffled Tube 1									
Shot #	Projectile	Projectile mass [g]	Mixture	ϕ	β	M_{avg}	F [N]	I_{exp}	I_{exp}-β
HS2278	P380-1.7BL-Al	264.71	1CH4 + 2O2 + 4.67N2	1.6	2.928	2.19	6713	2.72	0.93
HS2279	P380-1.7BL-Al	264.89	1CH4 + 2O2 + 4.67N2	1.4	2.928	2.24	6543	2.65	0.90
HS2280	P380-1.7BL-Al	264.97	1CH4 + 2O2 + 4.67N2	1.2	2.928	2.31	9385	3.82	1.30
HS2281	P380-1.7BL-Al	264.50	1CH4 + 2O2 + 4.67N2	1.0	2.928	2.33	9537	3.86	1.32
HS2292	P380-3BL	177.88	1CH4 + 2O2 + 4.67N2	1.0	2.928	2.50	13350	5.36	1.83
HS2293	P380-5BL	259.68	1CH4 + 2O2 + 4.67N2	1.0	2.928	2.34	13142	5.31	1.82
HS2294	P380-3BL	177.90	1CH4 + 2O2 + 4.67N2	1.0	2.928	2.48	18075	6.31	2.15
HS2299	P380-3BL	178.12	1CH4 + 2O2 + 4.67N2	1.0	2.223	2.72	13977	5.65	2.54
HS2300	P380-3BL	178.15	1CH4 + 2O2 + 4.67N2	1.0	2.223	2.81	14701	5.96	2.68
HS2302	P380-3BL	177.50	1CH4 + 2O2 + 4.67N2	1.0	2.223	2.83	17819	6.22	2.80
HS2303	P380-3BL	177.92	1CH4 + 2O2 + 4.67N2	1.0	2.889	2.67	12365	5.00	1.73
HS2305	P380-3BL	178.02	1CH4 + 2O2 + 4.67N2	1.0	2.889	2.79	16469	5.75	1.99

Baffled Tube 2									
Shot #	Projectile	Projectile mass [g]	Mixture	ϕ	β	M_{avg}	F [N]	I_{exp}	I_{exp}-β
HS2278	P380-1.7BL-Al	264.71	1CH4 + 2O2 + 4.67N2	1.6	2.223	2.39	9028	3.66	1.65
HS2279	P380-1.7BL-Al	264.89	1CH4 + 2O2 + 4.67N2	1.4	2.223	2.48	12239	4.95	2.23
HS2280	P380-1.7BL-Al	264.97	1CH4 + 2O2 + 4.67N2	1.2	2.223	2.58	13042	5.31	2.39
HS2281	P380-1.7BL-Al	264.50	1CH4 + 2O2 + 4.67N2	1.0	2.223	2.61	13773	5.57	2.51
HS2292	P380-3BL	177.88	1CH4 + 2O2 + 4.67N2	1.0	2.223	2.97	15188	6.10	2.75
HS2293	P380-5BL	259.68	1CH4 + 2O2 + 4.67N2	1.0	2.223	2.75	20586	8.32	3.75
HS2294	P380-3BL	177.90	1CH4 + 2O2 + 4.67N2	1.0	2.223	3.07	17245	6.02	2.71
HS2299	P380-3BL	178.12	1CH4 + 2O2 + 4.67N2	1.0	2.928	3.11	10857	4.39	1.50
HS2300	P380-3BL	178.15	1CH4 + 2O2 + 4.67N2	1.0	2.928	3.18	9613	3.90	1.33
HS2302	P380-3BL	177.50	1CH4 + 2O2 + 4.67N2	1.0	2.928	3.20	7809	2.72	0.93
HS2303	P380-3BL	177.92	1CH4 + 2O2 + 4.67N2	1.0	2.371	3.06	11915	4.82	2.03
HS2305	P380-3BL	178.02	1CH4 + 2O2 + 4.67N2	1.0	2.371	3.28	16500	5.76	2.43

Baffled Tube 3									
Shot #	Projectile	Projectile mass [g]	Mixture	ϕ	β	M_{avg}	F [N]	I_{exp}	I_{exp}-β
HS2278	P380-1.7BL-Al	264.71	1CH4 + 2O2 + 4.67N2	1.6	2.223	2.58	7326	2.97	1.34
HS2279	P380-1.7BL-Al	264.89	1CH4 + 2O2 + 4.67N2	1.4	2.223	2.73	9367	3.79	1.70
HS2280	P380-1.7BL-Al	264.97	1CH4 + 2O2 + 4.67N2	1.2	2.223	2.87	12606	5.13	2.31
HS2281	P380-1.7BL-Al	264.50	1CH4 + 2O2 + 4.67N2	1.0	2.223	2.90	11934	4.83	2.17
HS2292	P380-3BL	177.88	1CH4 + 2O2 + 4.67N2	1.0	2.223	3.40	14522	5.84	2.63
HS2293	P380-5BL	259.68	1CH4 + 2O2 + 4.67N2	1.0	2.223	3.12	14679	5.94	2.67
HS2294	P380-3BL	177.90	1CH4 + 2O2 + 4.67N2	1.0	2.223	3.51	14909	5.20	2.34
HS2299	P380-3BL	178.12	1CH4 + 2O2 + 4.67N2	1.0	2.223	3.42	11462	4.63	2.09
HS2300	P380-3BL	178.15	1CH4 + 2O2 + 4.67N2	1.0	2.223	3.46	10456	4.24	1.91
HS2302	P380-3BL	177.50	1CH4 + 2O2 + 4.67N2	1.0	2.223	3.48	11834	4.13	1.86
HS2303	P380-3BL	177.92	1CH4 + 2O2 + 4.67N2	1.0	2.370	3.40	12549	5.07	2.14
HS2305	P380-3BL	178.02	1CH4 + 2O2 + 4.67N2	1.0	2.370	3.64	9947	3.47	1.46

Baffled Tube 4									
Shot #	Projectile	Projectile mass [g]	Mixture	ϕ	β	M_{avg}	F [N]	I_{exp}	I_{exp}-β
HS2278	P380-1.7BL-Al	264.71	1CH4 + 2O2 + 4.67N2	1.6	2.258	2.77	9147	3.71	1.64
HS2279	P380-1.7BL-Al	264.89	1CH4 + 2O2 + 4.67N2	1.4	2.258	2.93	9217	3.73	1.65
HS2280	P380-1.7BL-Al	264.97	1CH4 + 2O2 + 4.67N2	1.2	2.258	3.10	10595	4.31	1.91
HS2281	P380-1.7BL-Al	264.50	1CH4 + 2O2 + 4.67N2	1.0	2.258	3.13	10994	4.45	1.97
HS2292	P380-3BL	177.88	1CH4 + 2O2 + 4.67N2	1.0	2.258	3.74	12186	4.90	2.17
HS2293	P380-5BL	259.68	1CH4 + 2O2 + 4.67N2	1.0	2.258	3.36	10193	4.12	1.83
HS2294	P380-3BL	177.90	1CH4 + 2O2 + 4.67N2	1.0	2.258	3.85	12629	4.41	1.95
HS2299	P380-3BL	178.12	1CH4 + 2O2 + 4.67N2	1.0	2.258	3.71	11933	4.83	2.14
HS2300	P380-3BL	178.15	1CH4 + 2O2 + 4.67N2	1.0	2.258	3.74	11897	4.83	2.14
HS2302	P380-3BL	177.50	1CH4 + 2O2 + 4.67N2	1.0	2.258	3.82	14023	4.89	2.17
HS2303	P380-3BL	177.92	1CH4 + 2O2 + 4.67N2	1.0	2.418	3.70	11162	4.51	1.87
HS2305	P380-3BL	178.02	1CH4 + 2O2 + 4.67N2	1.0	2.418	3.83	6509	2.27	0.94